UNIVERSIDADE DE LISBOA

FACULDADE DE CIÊNCIAS

DEPARTAMENTO DE BIOLOGIA VEGETAL

![Ciências ULisboa logo]

Spatial-Temporal distribution of phytoplankton biomass during a coastal upwelling episode obtained from remote sensing and *in situ* data

Pedro Miguel Ruela Ferreira Nunes

Mestrado em Ciências do Mar

Dissertação orientada por:
Profª. Doutora Vanda Brotas e Doutor Paulo B. Oliveira

2021

Agradecimentos / Acknowledgments

Resumo

Nos últimos anos, os blooms de algas nocivas tornaram-se um objeto de estudo importante para a comunidade científica devido ao crescimento mundial do fenómeno. Contudo, os blooms de algas não são necessariamente tóxicos, apesar de nocivos. Existem dois modos para serem considerados nocivos: a primeira é pela produção de toxinas pelas próprias algas; a segunda pela acumulação de biomassa que, por morte das células, provocam condições de anoxia (ausência de oxigénio), lesivas para o ecossistema. No entanto, os mecanismos físicos e biológicos que os desencadeiam não são totalmente conhecidos. Os mecanismos físicos (a temperatura da superfície do mar, a estratificação da coluna de água, o forçamento do vento, entre outros) controlam a biomassa fitoplanctónica possibilitando, em certos casos, uma acumulação da mesma devido à disponibilidade de nutrientes na coluna de água. Daí, é importante compreender de que forma os mecanismos físicos podem produzir as condições favoráveis ao aparecimento de blooms de algas nocivas. Um destes é o afloramento costeiro, mecanismo abordado na dissertação.

O objetivo da tese é o estudo da variação espácio-temporal da biomassa fitoplanctónica no Noroeste da Península Ibérica (Figueira da Foz, Portugal) durante um episódio de afloramento costeiro. De forma a avaliar a distribuição espácio-temporal do fitoplâncton recorreu-se a dados de deteção remota e dados *in situ* (concentração em clorofila-*a*, Chl-*a*, índice de biomassa do fitoplâncton), obtidos durante uma campanha oceanográfica de 12 a 19 de setembro de 2019. O presente trabalho foca as duas primeiras semanas de setembro de 2019, período no qual ocorreu uma campanha oceanográfica. Esta tese foi realizada no âmbito do Projeto HabWAVE, com o objetivo de estudar a formação dos blooms de algas nocivas no noroeste da costa portuguesa através de processos físicos e biológicos, aplicando os dados de deteção remota e *in situ*.

A primeira etapa do trabalho consistiu em verificar quais as imagens de satélite disponíveis, de onde foram analisadas as concentrações da clorofila-a (Chl-*a*) e a temperatura da superfície do mar (SST- *Sea Surface Temperature*). Em diversos dias houve ausência de imagens devido à cobertura nebulosa presente durante o mês de setembro de 2019. A SST foi igualmente obtida a partir da solução numérica do modelo ROMS. Recorreu-se a produtos de satélites com resoluções espaciais iguais ou inferiores a 1 km, para a concentração de clorofila-*a* e para a temperatura da superfície do mar. Por turno, o forçamento do vento e as correntes oceânicas foram obtidas a partir das soluções numéricas de diferentes modelos: o ECMWF-IFS e o ROMS, respetivamente. No caso dos produtos de clorofila-*a* fez-se uma análise prévia dos algoritmos disponíveis através da sua comparação com os dados *in situ* existentes (matchups). A análise dos matchups foi efetuada a partir de dois parâmetros estatísticos, o erro quadrático médio e o viés, que permitiram averiguar qual o produto de Chl-*a* mais apropriado para representar a sua variabilidade espacial na região de estudo. Com base nestes critérios foi selecionado o algoritmo de Chl-*a* "Piscismod Iberia" em relação aos algoritmos da Chl_NN e Chl_OC4Me (provenientes do sensor *Ocean and Land Colour Instrument* – OLCI), e do *Ocean Colour Climate Change Iniciative* (OC - CCI). O produto de SST selecionado é proveniente do sensor *Sea and Land Surface Temperature Radiometer* (SLSTR), do *Group of High Resolution Sea Surface Temperature* (GHRSST). Este sensor permite estimar a temperatura da superfície do mar através da calibração altamente precisa de três canais infravermelhos (S7-S8-S9).

Os resultados mostram sucessivos ciclos de intensificação e relaxamento do forçamento do vento favorável ao afloramento (componente *along-shore*) nas duas primeiras semanas de setembro de 2019. A variabilidade no campo do vento afeta a distribuição espacial da SST, ou seja, a intensificação da componente *along-shore* do vento produzirá uma intensificação do afloramento costeiro e um relaxamento do vento causará uma regressão do afloramento costeiro. A comparação entre as soluções

do modelo hidrodinâmico para a temperatura da superfície mostrou que o modelo reproduz valores semelhantes aos do satélite, no entanto, com uma subestimação dos valores da SST. A análise das distribuições de concentração de clorofila-*a* mostrou uma forte correlação com a distribuição espacial da SST, com elevados valores de Chl-*a* associados a baixos valores de SST. Contudo, a partir do dia 10 de setembro de 2019 em diante, observa-se que os valores elevados de clorofila-*a* não se associam necessariamente a temperaturas mais frias e em algumas áreas de baixa temperatura os valores de clorofila-*a* também são baixos. De forma a compreender este fenómeno estudou-se a variabilidade da costa para o largo (*cross-shore*), de onde se observou que a fraca concentração de clorofila-*a* está dependente da intensificação do forçamento do vento que, por sua vez, fortalece a componente *cross-shore* do transporte de Ekman. De acordo com a literatura, a interpretação sobre o desfasamento visual entre a Chl-*a* e a SST, observadas no dia 11 de setembro, dever-se-á à forte divergência, e consequentemente afloramento de águas subsuperficiais, induzida pelo aumento da componente *along-shore* do vento.

Posteriormente, analisaram-se, em pormenor, os dias 5, 10 e 11 de setembro, por apresentarem os maiores picos de ventos favoráveis ao afloramento costeiro. Nestes dias, a concordância visual entre as correntes oceânicas (modeladas pelo modelo ROMS) com a distribuição espacial da Chl-*a* e da SST mostraram que o modelo tem um melhor desempenho com as imagens de satélite para a distribuição espacial na região costeira, facto não verificado para o oceano aberto. De seguida, calcularam-se e comparam-se os campos da divergência horizontal que permitem inferir os locais onde o maior afloramento costeiro é mais intenso. O máximo de divergência costeira offshore observada é coincidente com as baixas concentrações clorofila-*a*, na mesma faixa de latitudes e longitudes. De seguida, três latitudes distintas (40.30°N, 40.19°N e 40.11°N) foram representadas em profundidade, para as correntes oceânicas e para a temperatura do mar. Com o decorrer do tempo foi visualizada uma progressão das camadas mais frias, associadas a uma intensificação do campo do vento. No caso das correntes oceânicas, uma componente maioritariamente para sul é observada em todos os dias. Contudo, nos dias 10 e 11, que correspondem aos dias de máxima intensidade do vento, verifica-se a formação de um jato costeiro confinado na região costeira. Logo, a baixa concentração de clorofila-*a* é justificada pela intensificação da componente *along-shore* do forçamento do vento que produz um máximo de divergência costeira. O máximo de divergência costeira observado não se encontra junto da linha costeira devido à interação entre a camada de Ekman da superfície e a camada de Ekman do fundo nas regiões menos profundas. Com a persistência do forçamento do vento, o campo de divergência vai progredir para fora com a evolução do afloramento costeiro. Por sua vez, permite a formação de um jato costeiro para sul coincidente com o sinal de baixa concentração de clorofila-*a* observada pelos dados de satélites.

Palavra-chave: Afloramento costeiro, Clorofila-*a*, SST, Campo de divergência horizontal, Deteção remota

Abstract

In recent years, harmful algal blooms have become an important object of study for the scientific community due to the worldwide growth of the phenomenon. However, algal blooms are not necessarily toxic, albeit harmful. There are two ways to be considered harmful: the first is by the production of toxins by the algae themselves; the second is due to the accumulation of biomass which, due to cell death, causes conditions of anoxia (lack of oxygen), which are harmful to the ecosystem. However, the physical and biological mechanisms that trigger them are not fully understood. Physical mechanisms (sea surface temperature, water column stratification, wind forcing, among others) control the phytoplankton biomass, enabling, in certain cases, its accumulation due to the availability of nutrients in the water column. Hence, it is important to understand how physical mechanisms can produce the conditions favourable for the emergence of harmful algal blooms. One of these is the coastal upwelling, a mechanism addressed in the dissertation.

The aim of this thesis is to study the spatiotemporal variation of phytoplankton biomass in the Northwest of the Iberian Peninsula (Figueira da Foz, Portugal) during an episode of coastal upwelling. In order to assess the spatiotemporal distribution of phytoplankton, remote sensing data and *in situ* data (chlorophyll-*a*, concentration, Chl-*a*, phytoplankton biomass index) were used, obtained during an oceanographic campaign from 12 to 19 September of 2019. The present work focuses on the first two weeks of September 2019, a period in which an oceanographic campaign took place. This thesis was carried out within the scope of the HabWAVE Project, with the aim of studying the formation of harmful algal blooms in the northwest of the Portuguese coast through physical and biological processes, applying remote sensing and *in situ* data.

The first stage of the work consisted of verifying which satellite images were available, from which the concentrations of chlorophyll-*a* (Chl-*a*), and the sea surface temperature (SST) were analysed. For several days there was an absence of images due to the cloudy coverage present during the month of September 2019. The SST was also obtained from the numerical solution of the ROMS model. Satellite products with spatial resolutions equal to or less than 1 km were used for the concentration of chlorophyll-a and for the temperature of the sea surface. In turn, the wind forcing, and ocean currents were provided by numerical solutions of different models, ECMWF-IFS, and ROMS, respectively. In the case of chlorophyll-a products, the available algorithms were previously analysed by comparing them with existing *in situ* data (matchups). The matchup analysis was performed using two statistical parameters (mean square error and bias) that allow us to determine which Chl-*a* product is most appropriate to represent its spatial variability in the study region. Based on these criteria, the Chl-*a* algorithm of Piscismod Iberia was selected in relation to the algorithms of Chl_NN and Chl_OC4Me (derived from the sensor Ocean and Land Colour Instrument - OLCI), and the Ocean Colour Climate Change Initiative (OC - CCI). The selected SST product comes from the Group of High-Resolution Sea Surface Temperature (GHRSST) sensor Sea, and Land Surface Temperature Radiometer (SLSTR). This sensor allows the estimation of sea surface temperature measurements through the highly accurate calibration of three infrared channels (S7-S8-S9).

The results show successive upwelling-favourable wind forcing intensification and relaxation cycles (along-shore component) in the first two weeks of September 2019. The variability in the wind field affects the spatial distribution of the SST, that is, the intensification of the along-shore component. shore wind will produce an intensification of the coastal upwelling and a relaxation of the wind will cause a regression of the coastal upwelling. The comparison between the hydrodynamic model solutions for surface temperature showed that the model reproduces values similar to those of the satellite, however, with an underestimation of the SST values. The concentration of chlorophyll-*a* was shown to correlate

with the spatial distribution of SST, with high Chl-*a* concentrations associated to low SST values. However, from September 10, 2019, onwards, it was observed that high chlorophyll-*a* concentrations are not necessarily associated with cooler temperatures, and that in some areas with low temperature the Chl-*a* values are also low. In order to understand this phenomenon, the variability of the coast to the sea (cross-shore) was studied, from which it was observed that the weak concentration of chlorophyll-*a* is dependent on the intensification of the wind forcing which, in turn, strengthens the cross-shore component of Ekman's transport. According to the literature, the interpretation of the visual lag between Chl-*a* and SST, observed on September 11th, should be due to the strong coastal divergence, and consequent upwelling of subsurface waters, induced by the increase in the along-shore component of the wind.

Subsequently, the 5th, 10th and 11th of September were analysed in detail, as they presented the highest peaks of favourable winds for the coastal upwelling. These days, the visual agreement between ocean currents (modelled by the ROMS model) with the spatial distribution of Chl-*a* and SST showed that the model performs better with satellite images for the spatial distribution in the coastal region, which is not true, for the ocean. Then, the horizontal divergence fields were calculated and compared, allowing to infer the places where coastal upwelling is stronger. The maximum observed offshore coastal divergence coincides with the low concentrations of chlorophyll-*a*, in the same range of latitudes and longitudes. Then, three distinct latitudes (40.30°N, 40.19°N and 40.11°N) were plotted in depth, for ocean currents and for sea temperature. Over time, a progression of the cooler layers was seen, associated with an intensification of the wind field. In the case of ocean currents, a mostly southerly component is observed every day. However, on days 10 and 11, corresponding to peak wind intensifies, a coastal jet confined to the coastal region is formed. Therefore, the low concentration of chlorophyll-*a* is justified by the intensification of the along-shore component of the wind forcing that produces a maximum of coastal divergence. The maximum observed coastal divergence is not found near the shoreline due to the interaction between the surface Ekman layer, and the bottom Ekman layer in the shallower regions. With the persistence of the wind forcing, the divergence field will progress offshore with the evolution of the coastal upwelling. In turn, it allows the formation of a coastal jet to the south coincident with the signal of low concentration of chlorophyll-a observed by satellite data.

Index

Table Index

Figure Index

of September 2019. The black rectangle represents the area where the mean was applied. Isothermal lines are separated by 0.5°C. The x-axis showed in the zonal profile represents the distance to the coast.

List of acronyms

AMSR-E: Advanced Microwave Scanning Radiometer for EOS
AVHRR: Advanced Very-High Resolution Radiometer
BAC: Baseline Atmospheric Correction
BPAC: Bright Pixel Atmospheric Correction
CDOM: Coloured Dissolved Organic Matter
Chl-*a*: Chlorophyll-a
CTD: Conductivity-temperature-depth
CZCS: Coastal Zone Colour Scanner
ECWAM: ECMWF Ocean Wave Model
ECMWF-IFS: European Center for Medium-range Weather Forecast – Integrated Forecasting System
Envisat: Environmental Satellite
EOS: Earth Observation System
ESA: European Space Agency
GAC: Global Area Coverage
GHRSST: Group for High Resolution Sea Surface Temperature
GOES: Geostationary Operational Environmental Satellites
HABs: Harmful Algal Blooms
HPLC: High Performance Liquid Chromatography
IFS: Integrated Forecasting System
IOCCG: International Ocean Colour Coordination Group
LAC: Local Area Coverage
MERIS: Medium Resolution Imaging Spectrometer
METOP-A: Meteorological Operation Satellite-A
MODIS: Moderate Resolution Imaging Spectroradiometer
MOS-1: Marine Observation Satellite-1
MSG: Meteosat Second Generation
MUR: Multi-scale Ultra-high Resolution
NASA: National Aeronautics and Space Administration
NIR: Near-Infrared Radiation
NOAA: National Oceanic and Atmospheric Administration
OC2: Ocean Chlorophyll 2-band algorithm
OC-CCI: Ocean Colour Climate Change Initiative
OCI: Ocean Colour Index
OCM-2: Ocean Colour Monitor-2
OISST: Optimum Interpolation Sea Surface Temperature
OLCI: Ocean and Land Colour Instrument
RAR: Real Aperture Radar
RMS: Root Mean Square
ROMS: Regional Oceanic Modelling System
S3A: Sentinel-3A
S3B: Sentinel-3B
SeaDAS: SeaWiFS Data Analysis System
SeaWiFS: Sea-viewing Wide Field-of-view Sensor
SEVIRI: Spinning Enhanced Visible and Infrared Imager
SLSTR: Sea and Land Surface Temperature Radiometer
SST: Sea Surface Temperature

SUOMI-NPP: Suomi National Polar-orbiting Partnership
TIROS-1: Television and Infrared Observation Satellite-1
VIIRS: Visible Infrared Imager Radiometer Suite
WFR: Water Full Resolution

Nomenclature / Symbols

$a_{phy}(443)$: Absorption coefficient at 443 nm

$a_{0,1,2,3}$: Empirical constants

$\rho_{490,560}$: Normalized reflectance ratio at wavelengths at 490 nm and 560 nm

ρ_{air}: Density of the air (kg/m^3)

Ψ: Root mean squared

δ: Bias

A_x: Coefficients

Cd: Empirical drag coefficient

$I_{Euphotic\ Zone}$: Light intensity in the euphotic zone (cd)

$I_{Surface}$: Light intensity in the surface (cd)

K_1, K_2: Parameters

$K_d(490)$: Diffuse Attenuation coefficient at 490 nm

$K_w(490)$: Diffuse Attenuation coefficient of pure water at a wavelength of 490 nm

N: Total number of samples

$R_{i,j}$: Irradiance-reflectance ratio of band I over the band j (nm)

Sat_i: Satellite

T_x: Wind stress along x direction (Pa or N/m^2)

T_y: Wind stress along y direction (Pa or N/m^2)

$|V|$: Wind velocity modulus (m/s)

V_x: Wind velocity along x direction (m/s)

V_y: Wind velocity along x direction (m/s)

Z_{eu}: Euphotic depth

Z^{st}: First optical zone

1 Introduction

Harmful algal blooms (HABs) appear frequently on the west coast of the Iberian Peninsula (Pinto et al., 2016), linked with the upwelling circulation occurring over the shelf (Oliveira et al., 2019). Toxic algae have devastating consequences on human society (for example health problems, contamination of aquaculture, leisure activities, etc.) as well as to the marine ecosystem (such as the death of marine species), so it is necessary to understand the dynamics such blooms. On the Portuguese coast, harmful algal blooms have been associated with the end of the coastal upwelling (Pitcher et al., 2010). Remote sensing plays an important role in the study of phytoplankton dynamics, ecosystem quality, and detection of harmful algal blooms (Blondeau-Patissier et al., 2014). A numerical model of ocean circulation to explain the physical and biological processes, necessary to trigger the production of harmful algae, and to predict the spatial and temporal progression of the phenomenon, has been proposed by Pinto et al., (2016), for the Iberian coast.

This thesis was developed in the frame of the HabWAVE Project, which aims to understand how the initiation of harmful algal blooms (in this case, the dinoflagellate *Gymnodinium catenatum* Graham, 1943) on the northwest coast of Portugal (Figueira da Foz) is associated with a set of physical and biological processes using the application of data from satellite and *in situ*.

1.1 Coastal Upwelling

Ekman (1905) proposed a theory, nowadays entitled Ekman Theory that explains the establishment of the coastal upwelling and the downwelling. The theory describes the movement of the ocean's surface layers due to frictional forces and the Coriolis effect exerted by the wind motion. The surface layers are deflected 45° to the right of the wind in the Northern Hemisphere (to the left of the wind in the Southern Hemisphere). As the water column is separated by different layers of water, a successive deflection of the subsequent layers with depth and a decrease in speed is observed, until it stops moving at a depth of approximately 100 meters. This process that is observed along the water column is called Ekman spiral and, when vertically integrated, mass transport of 90° to the right of the wind is obtained, called Ekman transport (Fig. 1.1).
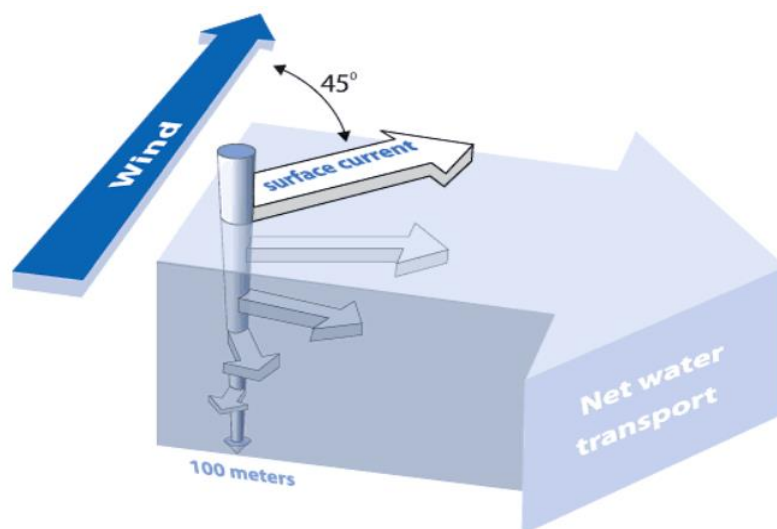
Figure 1.1: Representation of Ekman Theory. Adapted from https://oceanservice.noaa.gov/education/tutorial_currents/04currents4.html.

In the Northwest region of the Iberian Peninsula, the coastal upwelling occurs with the seasonal change in the position of the Azores High-pressure system during the summer, with the greatest intensity being

between May and October (Wooster et al., 1976). Fiúza et al., (1982) who studied the wind regime for Portugal for a period of 30 years (1931-1960) found that the coastal upwelling observed during July to September is due to the intensification and steadiness of northerly winds. With the strengthening of the northerly winds that blow parallel to the coastline, they will force an offshore Ekman transport in the surface layer creating, a divergence along the coast. In turn, to compensate for the divergence caused at the sea surface, cooler, nutrient-rich sub-surface waters emerge near the coast (Fig. 1.2), producing a geostrophic equatorward coastal current (Arístegui et al., 2009; Cunha, 2002).
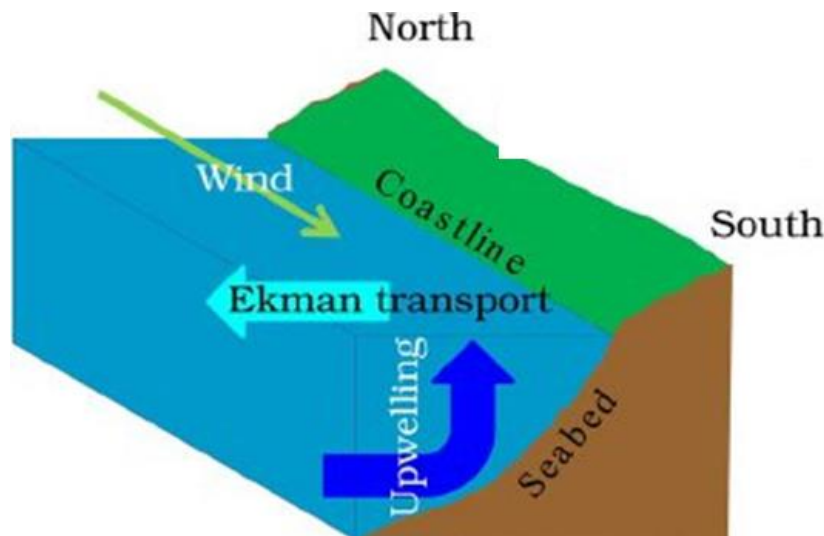
Figure 1.2: Representation of coastal upwelling in the northern hemisphere. Adapted from Zhang et al., (2012).

The coastal upwelling is important for its ability to influence spatially and temporally the dynamics of phytoplankton. One of the recurrent oceanographic structures in the Western Iberian is the formation of several cold water filaments, with the ability to exchange organic and inorganic matter between the coastal region and the open ocean. (Cravo et al., 2010; Relvas et al., 2007). It is important to know the dimensions, locations, and frequency of the filaments, in order to better understand the exchanges between the ocean and the coast (Cordeiro et al., 2015).

According to Strub et al., (1991), there are three possible mechanisms to justify the formation of filaments. The first one is the formation of filaments due to the existence of eddies that were observed in the west coast of North America. The second is due to irregularities in the shoreline and continental shelf that separate the alongshore currents, thus creating strong offshore flows. The third is due to the dynamic instabilities associated with the equatorward jet of the coastal upwelling.

Haynes et al. (1993), observed that the filaments formed in the capes were associated with topographic forcing that led to the separation of the coastal jet, while in the coastline without irregularities it was due to the evolution of frontal instabilities.

In the paper by Fiúza et al., (1983), it was stated that the observed coastal upwelling patterns were influenced by morphology and shelf/upper slope topography. In other words, it is difficult to describe an exact mechanism for the formation of filaments for the Northwest region of the Iberian Peninsula. One way to identify surface mesoscale circulation is to use SST products or numerical modelling solutions (Cordeiro et al., 2015).

1.2 Ocean colour remote sensing

Remote sensing is the acquisition of information about a property, a variable, in oppose to *in situ* or on-site observations (Sutcliffe et al., 2016). The use of satellites allowed for new and crucial knowledge on Earth (McCarthy et al., 2017) at different high resolution spatial-temporal scales.

Remote sensing originated in the 19th century, approximately 1859, with the use of a camera to photograph a French city (Petit Becetre) in a balloon by the Frenchman Gaspard Felix Tourmachon (Sutcliffe et al., 2016). However, it was in World War II that remote sensing made great technological advances (Fellous et al., 2001; Sutcliffe et al., 2016).

On October 4th, 1957, the first artificial satellite (Sputnik) was launched, marking a new era in Earth observation and space exploration (Chen et al., 2013; Sutcliffe et al., 2016). In 1960, the first meteorological satellite TIROS-1 (Television and Infrared Observation Satellite-1), from National Aeronautics and Space Administration (NASA), whose onboard equipment consisted of two televisions, was used to observe tropical storms (Fellous et al., 2001).

During the 1960s-1970s, the Soviet Union launched two satellites the Kosmos-243 (1963) and the Kosmos-384 (1970) that carried four microwave radiometers, enabling the collection of various data, such as the temperature of the sea surface and ice parameters (Fellous et al., 2001). During 1970, two ocean observation satellites, the Skylab (1973) and the GEOS-3 (1975), proved the concepts proposed in two conferences (Woods Hole Oceanography Institution - 1964 and Williamstown Conference - 1969) (Chen et al., 2013; Fellous et al., 2001).

In 1978, the first oceanographic satellite SeaSat-A was launched by NASA (Nayak et al., 2018; Sutcliffe et al., 2016). In the same period, the Nimbus-7 with the first Coastal Zone Colour Scanner (CZCS), as a proof-of-concept mission, validated the possibility to measure chlorophyll-*a* concentrations from space (Chen et al., 2013; Cracknell, 2018; Fellous et al., 2001). Taking into account the success of the Nimbus-7, which remained active for 8 years, as opposed to the predicted one year of operation (Cracknell, 2018). The CZCS collected data from the sea surface with an appropriate spatial, temporal, and spectral resolution, allowing the observation of the spatial variability of biological processes (Cracknell, 2018).

Starting in 1980, several satellites from different sets of countries were placed in orbit, for example, the Kosmos-1500 (with a real aperture radar (RAR)) from the Soviet Union, and MOS-1 (Marine Observation Satellite-1) from Japan (Fellous et al., 2001). This period was important because protocols were developed to validate the data collected by the satellite-borne sensors, and algorithms were created for atmospheric correction, and estimation of chlorophyll-*a* concentration at a global level (Chen et al., 2013).

On September 19th, 1997, the OrbView-2, with the SeaWiFS (Sea-viewing Wide Field-of-view Sensor) sensor, was launched with fundamental contributions to understand the variability of the marine ecosystem (Chen et al., 2013). The sensors MODIS Terra (1999), and MODIS Aqua (2002), with the ability to provide coverage of the global ocean on a daily scale (Chen et al., 2013). In recent years, several countries, and the European Union launched different satellites for ocean observation (Chen et al., 2013), such as MERIS/Envisat (Europe in 2002), OCM-2 (India in 2009), VIIRS/NPP (the United States of America in 2011), OLCI/Sentinel-3A and 3B (Europe in 2016 and 2018, respectively), etc. Currently, to study different physical and biological processes in the ocean it is necessary to select a satellite with an adequate spatial and temporal resolution, as seen in Fig. 1.3.
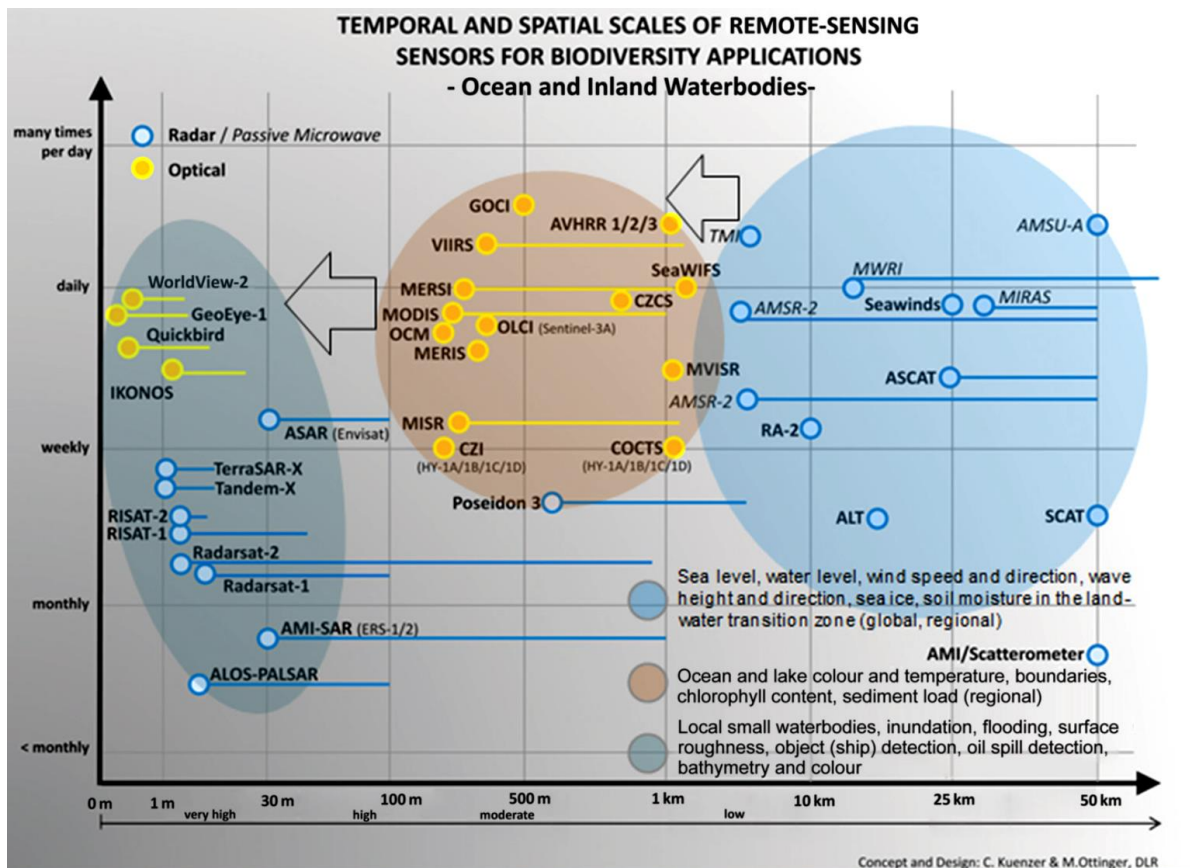
Figure 1.3: Spatial and temporal representation of remote sensing sensors with their respective applications. Yellow circles are optical, and infrared sensors, while blue circles are radar sensors. The turquoise, yellow, and blue ellipsoids represent the sensor applications for ocean and inland water bodies. The x-axes are the spatial resolution, and the y-axes are the temporal resolution. Adapted from Kuenzer et al., (2014).

1.3   Aim and objectives

This study aims to understand the spatial and temporal distribution of phytoplankton biomass during a coastal upwelling episode using both remote sensing and *in situ* data. To achieve this goal, the following questions were addressed: i) how the phytoplankton biomass and sea surface temperature responds to upwelling conditions; ii) how the cross-shore distribution varies temporally at selected latitudes; iii) how ocean currents and sea temperature vary in depth (from surface to 80 meters), according to the numerical model.

4

2   Data and Methods

The data used in the present work was obtained from various sources for the satellite data, model solutions, and the oceanographic campaign, as explained below.

2.1   Study Area and Sampling Campaign

The study area was located off Figueira da Foz (Portuguese northwest coast) (Fig. 2.1) between the longitudes 8.55°W and 9.60°W and latitudes 39.60°N and 40.80°N. *In situ* data was collected during an oceanographic campaign in Figueira da Foz held between the 12th and 19th of September of 2019, aboard the Hydrographic Institute's NRP Auriga vessel within the framework of the HabWAVE Project.
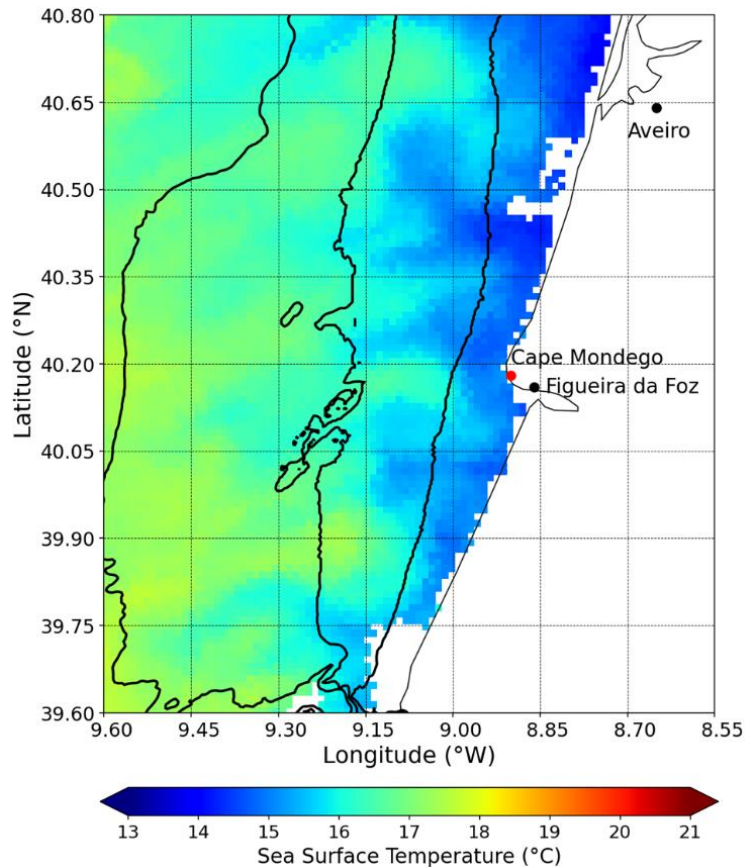
Figure 2.1: Representation of the study area (Figueira da Foz, Portugal) with the sea surface temperature (SST) for the 10th of September of 2019. The black lines represent the bathymetric of 50, 100 and 200 meters

The campaign aimed at the collection of water, sediment, and phytoplankton samples, and measure physical parameters along the zonal transect in Figueira da Foz. Various equipments measuring were utilized on board, such as a CTD (Conductivity-temperature-depth), and a Rosette sampler, as well as later in the laboratory, an HPLC (High Performance Liquid Chromatography) to determine photosynthetic pigments concentration in the water column (more detail in Santo, 2019). Concerning the laboratory analysis for this work, we only used the pigment Chl-*a*.

2.2   Satellite Data

For this study, several satellite-derived products were used, focusing on sea surface temperature and chlorophyll-*a* concentration. The figures were performed using Python software. The products used are described in Table 2.1

Table 2.1: Schematic table with satellite product details (product, platform/sensor, coverage, spatial resolution, temporal resolution, variable, processing level, and identification).

Product	Platform/Sensor	Coverage	Spatial Resolution	Temporal Resolution	Variable	Processing Level	Identification
GHRSST	Aqua / MODIS Aqua / AMSR-E CORIOLIS / WINDSAT Terra / MODIS NOAA-19 / AVHRR-3	Global	1 km	Daily	SST	4	MUR-JPL-L4-GLOB-v4.1
GHRSST	Aqua / MODIS MSG2 / SEVIRI Terra / MODIS NOAA-19 / AVHRR-3 METOP-A / AVHRR	Atlantic Ocean	1 km	Daily	SST	4	OISST_UHR_NRT-GOS-L4-MED-v2.0
OC-CCI	Aqua / MODIS Envisat / MERIS Orbview-2 / SeaWiFS SUOMI-NPP / VIIRS OLCI / S3A	Global	1 km	Daily	Chl-*a*	3	CCI_ALL-v5.0-1km-DAILY
-	SLSTR / S3A SLSTR / S3B	Global	1 km	Daily	SST	2	SL_2_WST__
-	OLCI / S3A OLCI / S3B	Global	300 m	Daily	Chl-*a*	2	OL_2_WFR__
-	OLCI / S3A OLCI / S3B	Iberia	300 m	Daily	Chl-*a*	3	Mass Concentration of Chlorophyll A in Sea Water – Iberia – Plymouth Marine Laboratory

Products were selected based on their spatial resolution, i.e., products with a resolution of one kilometre or less. Based on this requirement, the chosen products were: CCI ALL-v5.0-1km-DAILY, SL_2_WST, OL_2_WFr_, and Mass Concentration Chlorophyll A in Sea Water – Iberia – Plymouth Marine Laboratory. We chose not to select the products (MUR-JPL-L4-GLOB-v4.1 and OISST_UHR_NRT-GOS-L4-MED-v2.0) due to the difficulty in observing oceanographic processes in detail, because of the interpolation made to the data of the satellite.

Satellite data chosen were collected for the same area and study period, more specifically, from three databases: Copernicus Online Data Access (https://coda.eumetsat.int/#/home), Piscismod Data Viewer (https://piscismod.eofrom.space/) and Ocean Colour Climate Change Initiative (https://www.oceancolour.org/portal/). The database from Coda Eumetsat, satellite data from Sentinel-3 (3A and 3B) was obtained with the OLCI sensor and with a resolution of 300 m (Water Full Resolution - WFR) and from the SLSTR sensor, with a resolution of 1 km (High-Resolution Sea Surface Temperature). Both provided L2 products (applying a geophysical and atmospheric correction to data with the same resolution and location as the L1 product data). From the Piscismod portal/database, the downloaded data was L3 data (data resampled in a grid without distortion) from Sentinel-3 (Iberia region), OLCI sensor, with a resolution of 300 m. For the OC-CCI, the data is obtained by merging several sensors (MERIS, MODIS Aqua, SeaWiFS LAC & GAC, VIIRS, and OLCI - S3A), to produce a final product with a spatial resolution of 1 km and a processing level of L3[1].

2.2.1 Diffuse Attenuation coefficient

The KD490_MO7 product is the diffuse attenuation coefficient, i.e., the attenuation of light in the water column with depth. From this product the depth of the euphotic zone can be inferred. The formula to determine Kd used was proposed by Morel et al., (2007), is as follows:

$$K_d(490) = K_w(490) + 10^{(\sum_{x=0}^{n} A_x (log_{10}(\rho_{560}^{490})^x} \quad (1.1)$$

where $K_w(490)$ represents the value of pure water at a wavelength of 490 nm, ρ_{560}^{490} is the normalized reflectance ratio at wavelengths at 490 nm and 560 nm and A_x is the coefficient.

2.2.2 First Optical Depth and Euphotic Depth

The first optical depth (Z_1^{st}), according to Gordon & Ramnsey, (1975), is the layer of the water column in which 90% of the irradiance is reflected, also denominated as penetration depth (Z_{90}). For the case of the homogeneous ocean layer, the penetration depth can be represented as the inverse of the diffuse attenuation coefficient ($Z_{90} = Z_1^{st} \approx k^{-1}$). The depth of the optical is obtained by the following equation:

$$\ln(I_{Euphotic\ zone}) = \ln(I_{Surface}) - Kd(490) * Z_{eu} \quad (1.2)$$

Where $\ln(I_{Euphotic\ zone})$ is the light intensity in the euphotic zone, $\ln(I_{Sur})$ is the light intensity in the surface, Kd(490) is the Diffuse Attenuation coefficient provided by the satellite and Z_{eu} is the euphotic depth.

The euphotic layer goes from the surface to the depth at which the luminous intensity is reduced to 1% of its value on the surface (Kirk,1994). In other words, the first optical zone, Z_1^{st}, can be calculated using the relation with the euphotic zone by rewriting the previous equation:

---

[1] L1, L2, L3, and L4 correspond to the processing level that the satellite data receive.

$$Z_1^{st} = \frac{Z_{eu}}{4.6} \quad (1.3)$$

2.2.3 Ocean Colour algorithms

Several algorithms have been developed over the years to retrieve chlorophyll-*a* concentration (Werdell et al., 2018). Only four are described here in detail: the Chl_NN, and Chl_OC4Me (applied to sensor OLCI of Sentinel-3A and 3B), the Piscismod Iberia, and the OC-CCI. The last two use Sentinel-3; however, the Piscismod Iberia uses the Sentinel-3A and 3B, while OC-CCI uses only Sentinel-3A.

2.2.3.1 Chl_OC4Me

The Chl_OC4Me algorithm is a semi-analytical model developed by André Morel et al., (2007), for MERIS. This algorithm uses Baseline Atmospheric Correction (BAC) using NIR reflectance assuming that the pixels are black for clear waters with multiple scattering aerosols (Antoine & Morel, 1999) in conjunction with Bright Pixel Atmospheric Correction (BPAC) (Moore et al., 1999). It is an algorithm with a preferred application for type I waters, whereas, in type II waters it tends to overestimate chlorophyll concentration and in regions contaminated by sun glint (A Morel & Antoine, 2011). The equation to calculate the chlorophyll concentration is:

$$log_{10}[Chl] = \sum_{x=0}^{n} (A_x * (log_{10}(R_j^i)^x \quad (1.4)$$

Where R_j^i is the irradiance-reflectance ratio of band I (443, 490, and 510 nm) over band j (560 nm), and the A_x are the coefficients obtained empirically, (more detail in André Morel et al., 2007).

For a more in-depth description of these algorithms, uncertainties and atmospheric corrections can be found in (Antoine, 2010).

2.2.3.2 Chl_NN

The algorithm Chl_NN use the method Inverse Radiative Transfer Model – Neural Network to estimate the normalized reflectance of the different OLCI bands, having been developed for type II waters due to their composition and optical properties that depend on other parameters besides Chl-*a*, namely suspended particulate matter and organic matter concentration (CDOM) (Doerffer, 2010; Schiller & Doerffer, 1999). The Neural Network algorithm uses Alternative Atmospheric Correction as an atmospheric correction (ESA & EUMETSAT, 2018). This atmospheric correction uses top of atmosphere reflectances, corrected absorbing gases, and observation geometry to estimate water-leaving reflectances and atmospheric parameters (Giannini et al., 2021). Then, the neural network is trained and tested with various angle-dependent radiance spectra simulations using HYDROLIGHT (Mobley, 1999). The formula used to calculate chlorophyll-*a* (Doerffer, 2010) is as follows:

$$Chl = k_1 * (a_{phy}(443))^{k_2} \quad (1.5)$$

where $a_{phy}(443)$ represents the absorption coefficient at 443 nm wavelength, and k_1 to k_2 are parameters.

A more in-depth description of these algorithms, uncertainties, and atmospheric corrections can be found in (Doerffer, 2010).

2.2.3.3 Piscismod Iberia

The Piscismod Iberia Sentinel 3 product is produced using the Polymer atmospheric correction and the built in Chl-*a* algorithm (Steinmetz et al 2011). The chlorophyll-*a* product is obtained by the ocean colour algorithm OC2 (Ocean Chlorophyll 2-band algorithm), initially developed for SeaWiFS (O´Reilly et al., 1998), and by Polymer (atmospheric correction), applied for MERIS (Steinmetz et al., 2011). The OC2 is an empirical equation that uses the ratio of remote sensing reflectance at 490 nm and 555 nm, proposed by Aiken et al., (1995), to estimate chlorophyll-*a* concentrations (O´Reilly et al., 1998). The formula proposed by O'Reilly et al., (1998, 2000) is as follows:

$$Chl = 10^{(a_0 + a_1 R_2 + a_2 R_2^2 + a_3 R_2^3) + a_4} \quad (1.6)$$

Where $R_2 = \log_{10}(R_{555}^{490})$, a_0, a_1, a_2, a_3, and a_4 are empirical constants with values of 0.341, -3.001, 2.811, -2.041, and -0.04, respectively.

The Polymer is an atmospheric algorithm able to retrieve information on ocean colour that is contaminated by the presence of sun glint (one of the main strengths), and aerosol (Steinmetz et al, 2018; Wang et al., 2020; Sandoval et al., 2019). This algorithm uses a spectral matching method (spectral optimization method) that applies the atmospheric correction to all spectral bands (Steinmetz et al, 2011; Frouin et al., 2012), to remove the atmospheric and surface components of the water reflectance signal.

2.2.3.4 OC-CCI

Through the Ocean Colour Climate Change Initiative interface, the product of chlorophyll-*a* concentration in seawater (version 5.0) was transferred. The product OC-CCI had to resort to merging processes that include band-shift and bias-corrected correction of the various sensors, to be able to compare the satellite data with each other. There have been several versions, we used version 5. The chlorophyll-*a* product was generated by SeaDAS (SeaWiFS Data Analysis System) through the combination of four algorithms: the OCI (ocean colour index from Hu et al., 2012), the OCI2 (refined ocean colour index from Hu et al., 2019), the OC2 (ocean colour chlorophyll 2-band from O'Reilly et al., 1998), and OCx, depending on the water classes (Jackson et al, 2017).

2.3   Quality Control

The satellite data, to be correctly interpreted, requires going through quality control verification. Thus, specific masks were applied to the various products of chlorophyll-*a* (CHL_OC4ME, and CHL_NN), and diffuse attenuation coefficient, provided by ESA.

Table 2.2: List of masks used for chlorophyll-*a*, suspended matter, and attenuation coefficient. Adapted from EUMETSAT, 2019.

Product names	Products	Common flags	Processing chain flags	Product flags
Water leaving reflectances – Open Waters	Oa**_reflectance → Oa**_reflectance	Ocean Colour Products (WATER *or* INLAND_WATER) *and not* (CLOUD CLOUD_AMBIGUOUS CLOUD_MARGIN INVALID COSMETIC SATURATED SUSPECT HISOLZEN HIGHGLINT SNOW_ICE)	Open Water products	*none*
Algal pigment concentration – Open Waters	chl_oc4me → CHL_OC4ME		*not* (AC_FAIL WHITECAPS ANNOT_ABSO_D ANNOT_MIXR1* ANNOT_DROUT* ANNOT_TAU06 RWNEG_O2 RWNEG_O3 RWNEG_O4 RWNEG_O5 RWNEG_O6 RWNEG_O7 RWNEG_O8)	*not* OC4ME_ FAIL
Diffuse attenuation coefficient – Open Waters	trsp → KD490_M07			*not* KDM_FAIL
Photosynthetically Active Radiation – Open Waters	par → PAR			*not* PAR_ FAIL
Aerosol Optical Thickness and Ångström exponent – Open Waters	w_aer → T865, A865			*none*
Algal pigment concentration – Complex Waters	chl_nn → CHL_NN		Complex Water Products *no specific flags to be applied*	*not* OCNN_FAIL
Total suspended matter concentration – Complex Waters	tsm_nn → TSM_NN			*not* OCNN_FAIL
Coloured Detrital and Dissolved Material absorption – Complex Waters	iop_nn → ADG443_NN			*not* OCNN_FAIL
Integrated Water Vapour Column	iwv → IWV	Atmospheric Products	Water Vapour over WATER *not* MEGLINT	*not* WV_FAIL

In the Table 2.2, the products of Algal pigment concentration – Open Waters and Complex Waters, and Diffuse attenuation coefficient were implemented the following common flags: Cloud, Cloud_Ambiguous, Cloud_Margin, Invalid_Cosmetic, Saturated, Suspected Hisolzen, and Highlight. In the case of the Open Waters all the specific processing chain flags were performed and the product flags: OC4ME_Fail. The Complex Water Products does not have any specific flag to be applied, from the processing chain flags. It was applied the product flags: OCNN_Fail. In certain images, it was observed some incorrect applications of the flags, such as inaccurate signalization of cloud pixels and negative values of reflectance associated with errors in an atmospheric correction, in coastal regions.

This is referred to in "Product Notice" (Eumetsat, 2019), where it is pointed out that the masked products in coastal areas exhibit a lower quality and residual limitations.

For the sea surface temperature data (SST), quality control was carried out using the following formula:

$$If = quality\ control < 4\ then\ NaN\ else\ sea_{surface_{temperature}} - 273.15\ (1.7)$$

Table 2.3: Quality control for sea surface temperature pixels. Adapted from https://sentinel.esa.int/web/sentinel/technical-guides/sentinel-3-slstr/level-2/sea-surface-temperature-ghrsst.

Numeric Code	Text Code	Description
0	No_data	No data
1	Cloud	Cloud contaminated data
2	Worst_quality	Worst quality of useable data
3	Low_quality	Low quality of useable data
4	Acceptable_quality	Acceptable quality useable data
5	Best_quality	Best quality useable data

Quality Level code

When we implement this equation (1.7) to the product of SST, it provides information about the pixels without data and with the best quality, respectively 0 and 5. Therefore, we obtain a final product with a higher quality level and accuracy.

2.4   Model Solutions

The model solutions come from numerical models of atmospheric and oceanic circulation, described in detail in the next sections. These were used with the aim of having synergy between the models and the satellite data, and to interpret the pattern observed in the satellite images, in the presence of satisfactory results.

2.4.1   Oceanic circulation models

The model solutions were selected to provide information on the same physical parameters as observed in the satellite data, such as sea surface temperature, but also on chlorophyll-*a* concentration. The models were analysed using Python software. Table 2.4 presents the information referring to the models in greater detail.

Table 2.4: Schematic table with model products details (Model, Platform/Sensor, Coverage, Spatial Resolution, Temporal Resolution, Variable, Processing Level, and Identification).

Model	Coverage	Spatial Resolution	Temporal Resolution	Variables	Processing Level	Identification
ROMS	Figueira da Foz	3 km	Daily	SST Chl-*a*	4	roms_LD_UA_12h_FFoz_3km_201909
ROMS	Figueira da Foz	1 km	Daily	SST	4	roms_his_PercNew2mn3r_FFoz_201905-09_temp_srho45
ROMS	Figueira da Foz	1 km	Daily	SST Chl-*a*	4	roms_LD_UA_12h_FFoz_1km_201909

The model fields selected for this work were the obtained from the ROMS solutions provided by the Ocean Modelling Group from the University of Aveiro because they had a spatial resolution of 1 km, therefore similar to the satellite products. The fine resolution of the model enabled a more rigorous comparison with remote sensing data and the characterization of coastal processes (inner-shelf circulation). The ROMS Regional Oceanic Modelling System model is a split-explicit, 3D free-surface, sigma-coordinate, developed for regional applications (Shchepetkin and McWilliams, 2003; Shchepetkin and McWilliams, 2005). ROMS solves primitive equations using Boussinesq and hydrostatic vertical momentum balance (Penven et al., 2006). The model configuration is the same as

used in Nolasco et al. (2013), with a horizontal resolution (~1 km in longitude) and different physical and biological variables solved by the model.

2.4.2 Atmospheric circulation models

The atmospheric model solutions for the wind speed were obtained from the European Center for Medium-range Weather Forecast – Integrated Forecasting System (ECMWF-IFS) with a spatial resolution of 10 km at 6 hourly intervals. The IFS provides weather forecasts by including the spectral wave model ECWAM with the parameterizations of physical processes in the atmospheric boundary layer and the land surface (Guillou et al., 2017; Watson et al., 2015).

2.4.2.1 Wind Stress

To calculate the along-shore (Ty) and cross-shore (Tx) components of the wind on the sea surface, the following bulk formula was used:

$$T_x = \rho_{air} C_d |\vec{v}| * v_x \quad (1.8)$$

$$T_y = \rho_{air} C_d |\vec{v}| * v_y \quad (1.9)$$

Where, ρ_{air} is the density of the air (1.225 kg/m^3), C$_d$ is the empirical drag coefficient, $|\vec{v}|$ is the magnitude, v$_y$ is the estimated value of the along-shore component and v$_y$ is the estimated value of the along-shore component. The drag coefficient has a value of 0.0013 to estimate upwelling through six-hourly surface pressure fields (Bakun et al., 1975; Schwing et al., 1996). Then, a 40-hour low-pass filter was applied to filter out the influence of sea breeze and land breeze.

2.5 Statistical Analysis

To assess the quality of the algorithms in comparison with the *in situ* data, a statistical analysis was performed. The statistical parameters used were linear regression: correlation coefficient (r^2), intercept, and slope. For the error estimate parameters: root mean squared (Ψ) and bias (δ), were calculated with the following formulas.

$$\Psi = \frac{1}{N} \left(\sum_{i=1}^{N} [\log(Sat_i) - \log(In\ situ_i)]^2 \right)^{\frac{1}{2}} \quad (1.10)$$

$$\delta = \frac{1}{N} \sum_{i=1}^{N} [\log(Sat_i) - \log(In\ situ_i)] \quad (1.11)$$

N is the total number of samples, i is the sample index, Sat is the value obtained from satellite data. The objective of Ψ is to quantify the precision/dispersion of the data and δ to evaluate its deviation concerning the real value. The results concerning the statistical analysis are presented on a logarithmic scale since bio-optical data tends to be represented using a lognormal distribution model (Campbell et al., 1995).

3   Results

3.1   Data Validation

3.1.1   Chlorophyll-*a* Matchups

The selection of satellite data and numerical solutions was based on products with the highest spatial resolution, that is, products with a spatial resolution between 1 km and 300 m. The selected products that fulfilled the requirements, from the Table 2.1 and 2.4, were: Chl_NN, and Chl_OC4Me (from OLCI sensor), OC-CCI, Piscismod Iberia, roms_his_Perc, and roms_LD_UA. To quantify the product with the best quality for the study area, two statistical parameters were used, using *in situ* data together with satellite data.

To compare the *in situ* data with the satellite data, it was necessary to apply equations 1.2 and 1.3 to calculate the 1st optical layer and the euphotic layer based on the product of the attenuation coefficient.

Table 3.1: Schematic table with the values of the 1st optical depth and the euphotic depth based on the product of the attenuation coefficient for the 12th and 14th of September 2019.

Sentinel-3B (12/09/2019)					
Label	**Lon [°W]**	**Lat [°N]**	**KD490_M07 [m^{-1}]**	**Euphotic depth [m]**	**First optical depth [m]**
A01	-9.24	40.21	0.169	27.190	5.911
10	-9.25	40.22	0.174	26.460	5.752
12	-9.12	40.22	0.299	15.560	3.340
13	-9.12	40.22	0.299	15.560	3.340
15	-8.95	40.22	0.205	22.477	4.886
A02	-8.96	40.21	0.205	22.477	4.886
Sentinel-3A (14/09/2019)					
Label	**Lon [°W]**	**Lat [°N]**	**KD490_M07 [m^{-1}]**	**Euphotic depth [m]**	**First optical depth [m]**
B01	-8.86	40.15	-	-	-
16	-8.90	40.16	-	-	-
18	-8.91	40.17	-	-	-
20	-8.92	4.022	0.189	24.387	5.302
22	-8.95	40.22	0.184	25.060	5.448
24	-9.00	40.22	-	-	-
28	-9.11	40.22	-	-	-
31	-9.24	40.22	0.248	18.580	4.039
34	-9.38	40.22	0.205	22.477	4.886

In table 3.1 the Z_1^{st} had values up to 6 meters in depth, while the depth of the euphotic layer reached 27.20 meters, on the 12th of September 2019. For the 14th, the depth of the 1st optical layer reached 5.30 meters and the depth of the euphotic layer reached 25.05 meters.

As the Z_1^{st} reached a maximum of 6 meters, *in situ* data collected at 5 meters were used alongside the satellite data that is provided in Table 3.2.

Table 3.2: Schematic table with the values of the total chlorophyll-*a in situ* and the values of chlorophyll-*a* products from OLCI (Chl_NN, and Chl_OC4Me), Piscismod Iberia, and OC-CCI for 12th and 14th of September 2019.

Chlorophyll-*a* [*in situ*]					OLCI		Piscismod Iberia	OC-CCI
Label	Lon [°W]	Lat [°N]	Date	Tchl*a* [µg/L]	Chl_NN [mg/mg³]	Chl_OC4ME [mg/mg³]	Chl-*a* [mg/mg³]	Chla-*a* [mg/mg³]
10	-9.25	40.22	12/09/2019	2.1656	0.8650	3.0774	2.7155	2.3583
12	-9.12	40.22	12/09/2019	4.4308	0.8650	3.0774	2.7155	2.3583
15	-8.95	40.22	12/09/2019	3.3354	1.3365	3.6892	2.3759	2.5752
B01	-8.86	40.15	14/09/2019	0.3199	-	-	-	-
16	-8.90	40.16	14/09/2019	0.9471	0.3134	-	1.4509	-
18	-8.91	40.17	14/09/2019	1.3107	0.3369	-	1.9466	-
20	-8.92	4.022	14/09/2019	0.8509	0.3249	3.8254	2.4838	3.6133
22	-8.95	40.22	14/09/2019	6.0205	1.1149	3,6892	3.6903	4.3413
24	-9.00	40.22	14/09/2019	5.9372	0.7482	-	3.3026	5.7669
28	-9.11	40.22	14/09/2019	3.7804	0.6472	-	2.7750	2.8317
31	-9.24	40.22	14/09/2019	0.7679	0.3623	3.9667	1.9562	2.1178
34	-9.38	40.22	14/09/2019	0.6836	0.3757	4.1131	1.7232	2.0594

Using the data from Table 3.2, equations 1.10 and 1.11 were used to obtain various statistical parameters. With the obtained statistical parameters, it is possible to identify which of the product of chlorophyll-*a* data (Chl_NN, and Chl_OC4Me, Piscismod Iberia, and OC-CCI) presents the most accurate information.
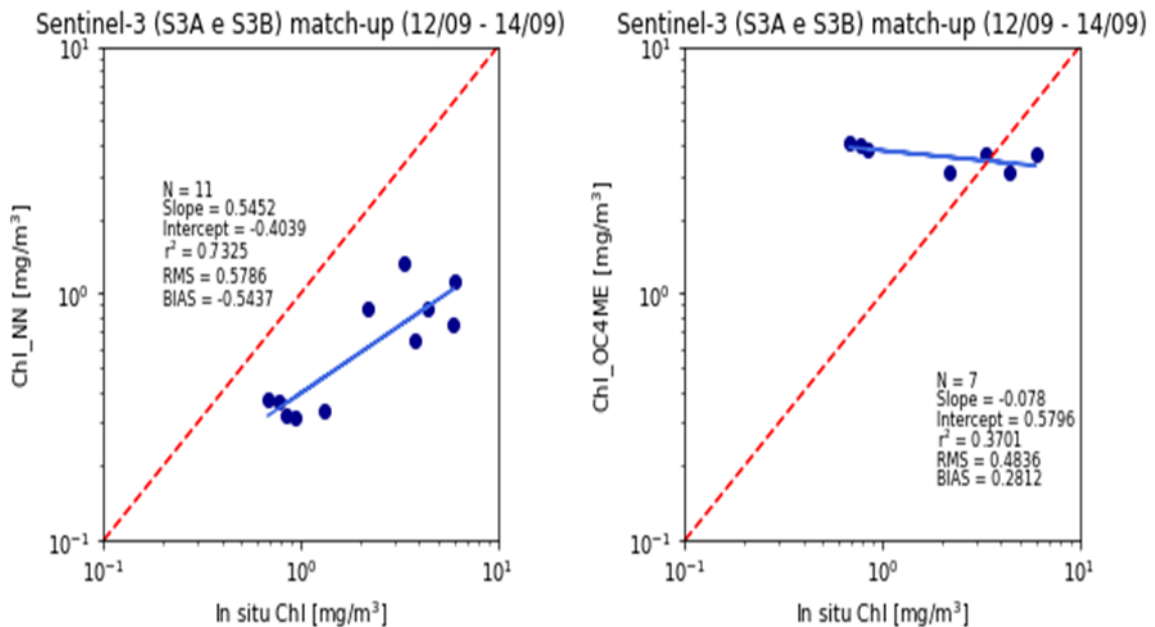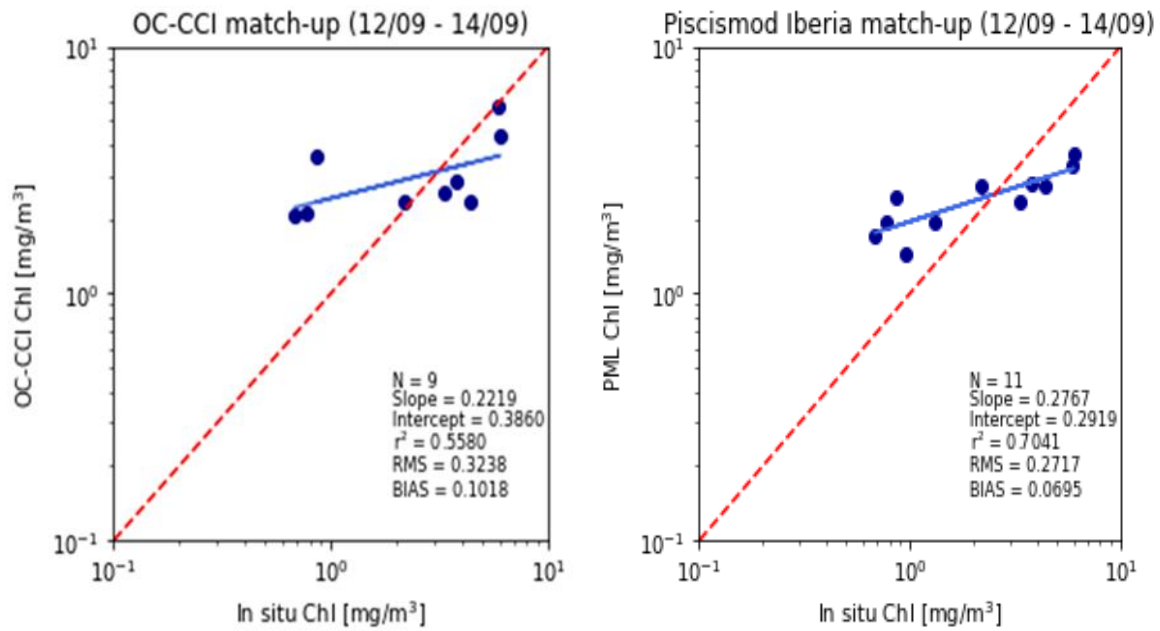
Figure 3.1: Comparison of chlorophyll-*a in situ* data with satellite data. The left image is from the "Neural Network" algorithm, the right image is the "OC4Me" algorithm, the bottom right image is the Piscismod Iberia algorithm, and the bottom left image is the "OC-CCI" algorithm.

By analyzing the graphs, we can see that the chlorophyll-*a* algorithm "Neural Network" has the best data correlation, with an $r^2 = 0.73$, followed by PML chlorophyll-*a* based on the "Polymer" with $r^2 = 0.70$, second to last the "OC-CCI" with $r^2 = 0.56$ and, finally, the chlorophyll-*a* "OC4Me" with an $r^2 = 0.37$. Using the root mean square error and bias error statistical parameters, we observe that the best is the PML Chl with a $\Psi = 0.27$ and $\delta = 0.07$, that is, the data predicted by the algorithm have a small dispersion and are little overestimated concerning the other two models ("Neural Network" and "OC4Me"). The OC-CCI model is the second-best product with a $\Psi = 0.32$ and $\delta = 0.10$, with values like to the product of the Piscismod Iberia. The "Neural Network" model has values of $\Psi = 0.58$ and $\delta = -0.54$ (data from this algorithm is underestimated) and the "OC4Me" model has values of $\Psi = 0.48$ and $\delta = 0.28$.

3.1.3 Satellite and Model Comparisons

The satellite SST data was compared with the numerical solutions two ROMS configurations: ROMS_Perc and ROMS_LD. The results for the sea surface temperature are summarized in Table 2.4, (roms_LD_UA_12h_FFoz_1km and roms_his_PercNew2mn3r_FFoz), this comparison aims at the selection of the model that most accurately reproduces reality using quantitative analysis.

Figure 3.2: Quantitative analysis of sea surface temperature based on a latitudinal mean along a longitudinal transect for the 11th of September 2019. The red line is the SST from the satellite data, the orange line is SST from the numerical solution of roms_LD_UA_12h_FFoz_1km and the blue line is SST from the numerical solution of roms_his_PercNew2mn3r_FFoz. The x axis represents the longitude, the y-axis is the sea surface temperature (units: °C), and the lines illustrates the latitudinal mean (40.40°N-40.35°N) for the SST values.

The cross-shore SST profile (Fig. 3.2) demonstrates how the sea surface temperature varies from offshore to the coastal region for the 11th of September 2019. In the oceanic region (9.6°W), the SST (satellite data – red line) has a maximum value of 16.4°C. Nonetheless, as we approach the coastal region the temperature decreases until reaching a minimum of 14.0°C (around 8.93°W). That is, there was a variation of 2.4℃ from offshore to the inner shelf (between 9.60°W and 8.93°W). From 8.93°W to the coast, there was an increase in temperature with a maximum of 15.0°C.

The numerical solution graph (roms_LD_UA – orange line) represents a similar temperature behaviour compared to the satellite graph, however, there are visible differences between the two graphs. The main differences are evident from 9.1°W coastward, where the model shows a slight increase in temperature to 14.8°C compared to the satellite's 14.4°C. From 9.1°W to 8.93°W, the blue line shows a marked decrease in temperature with values of 13.5°C, that is, it has a difference of 0.5°C concerning the satellite graph. From 8.93°W towards the coast, the temperature exhibits a significant increase with values around 16.0°C. At 9.6°W the numerical solution displays higher values in the order of 1.0°C compared to the satellite.

The model (roms_his_Perc - blue line) behaves similarly to the other graphs, in terms of a decrease in temperature down to 8.93°W and, followed by an increase in temperature in the coastal region. However, the biggest difference of this model relating to the other two graphs is that the temperature from offshore to the coastal region is higher, for example, the temperature in the oceanic region is 18.0°C instead of

around 16.4°C and the temperature decrease, at 8.93°W, reaches 16.3°C instead of 14.0°C - 13.5°C. Considering these factors, we selected the numerical solution (roms_LD_UA) because it can reproduce more accurately the sea surface temperature.

Given that the roms_LD_UA also provided Chl-*a* concentrations estimates, we compared the numerical solution (roms_LD_UA) with satellite data for the concentration along a cross-shore profile.
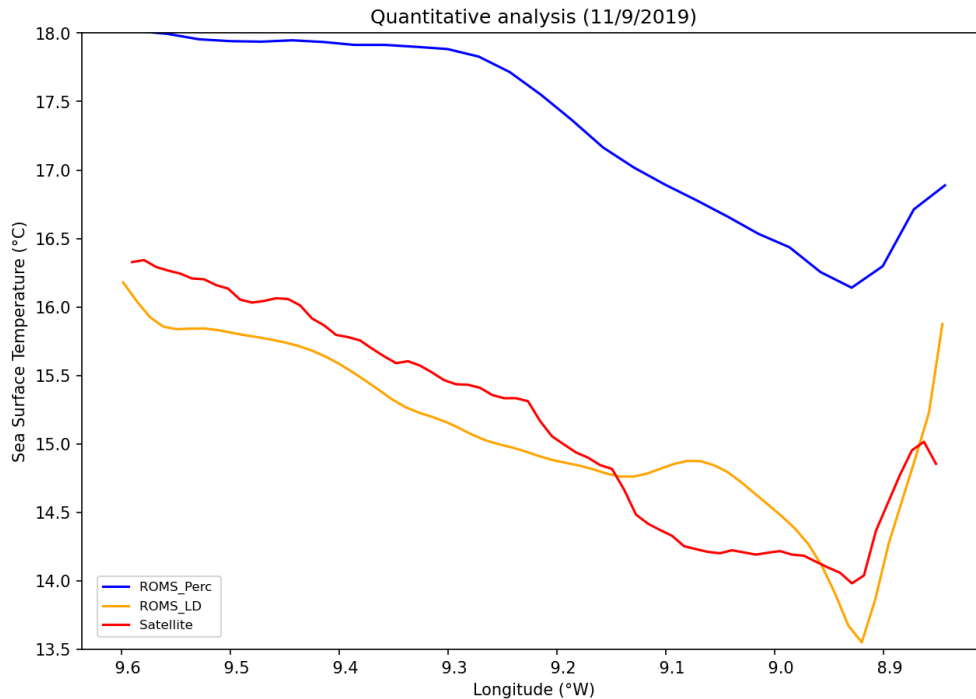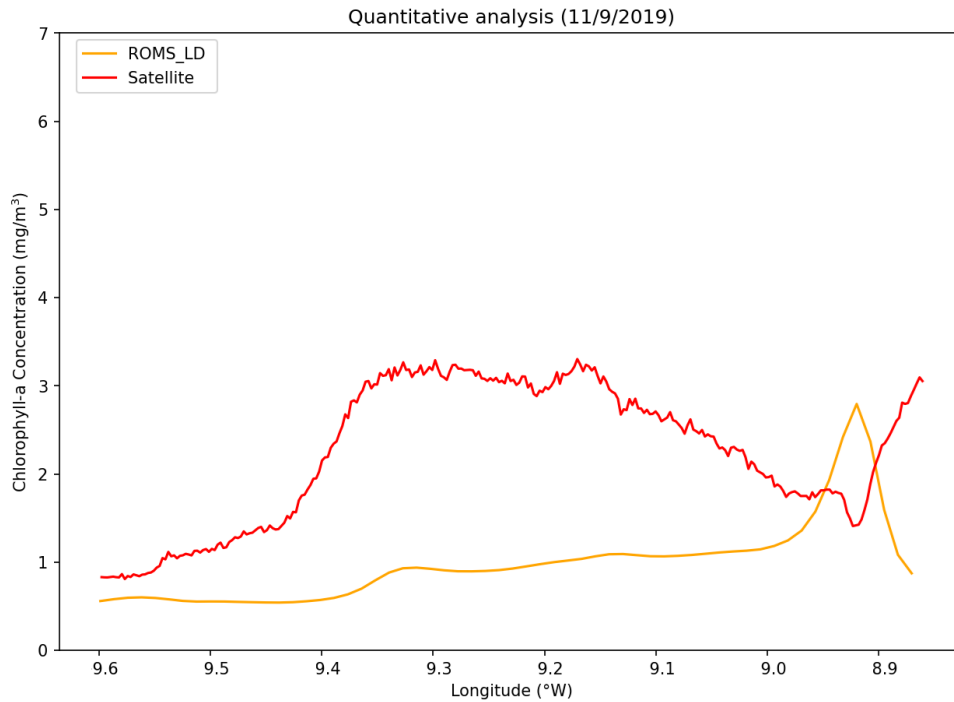

Figure 3.3: Quantitative analysis of chlorophyll-*a* concentration based on a latitudinal mean along a longitudinal transect for the 11th of September 2019. The red line is the Chl-*a* from the satellite data, the orange line is Chl-*a* from the numerical solution of roms_LD_UA_12h_FFoz_1km. The x-axis represents the longitude, the y-axis is the chlorophyll-a concentration (units: mg/m^3), and the lines illustrates the latitudinal mean (40.40°N-40.35°N) for the Chl-*a* values.

Fig. 3.3 shows how the concentration of chlorophyll-*a* varies from the oceanic region to the coast. In the satellite graph, we can see that the offshore region has a concentration of chlorophyll-*a* with values below 1 mg/m^3. As we approach the coastal region, the chlorophyll-*a* values increase to values between 4 mg/m^3 and the 3 mg/m^3. However, between 9.0°W and 8.9°W, the concentration of chlorophyll-*a* is below 2 mg/m^3 before increasing again to values above 3 mg/m^3 near the coast. In the case of the model, the concentration of chlorophyll-*a* increases slowly, remaining below 2 mg/m^3 until around 9.0°W, in contrast to the sharp increases observed in the satellite data. Furthermore, the big difference between the model and the satellite occurs between the longitudes of 9.0°W and 8.9°W, with the model assuming a maximum of chlorophyll-*a* with values of 3 mg/m^3, while the satellite represents a minimum of chlorophyll-*a* below 2 mg/m^3. Based on this representation, it was decided not to use the numerical solution of chlorophyll-*a*.

3.2 The upwelling episode

The *in situ* observations were carried out during the relaxation phase of a strong upwelling-favourable wind pulse. This episode is described with more detail in the next sections.

3.2.1 Wind Forcing

To study the coastal upwelling episode, it is necessary to observe the wind forcing for the first 21 days of September 2019, with greater detail for the along-shore/upwelling-favourable component. The information regarding the wind intensity (along-shore, T_y) in September 2019 is represented in figure 3.4.
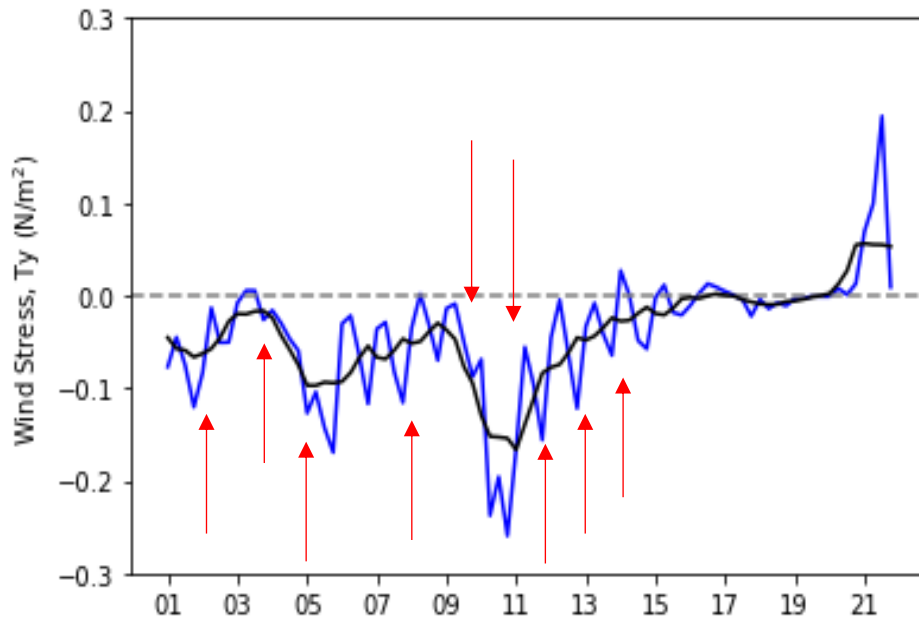
Figure 3.4: Wind stress intensity (along-shore, T_y) for the first 21 days of September 2019. The blue line represents unfiltered wind data, and the black line represents wind data with a low-pass filter (40 hours). The red arrow indicated the study days with could-free images (2, 4, 5, 8, 10, 11, 12, 13, and 14 of September 2019). The x-axis represents the days, and the y-axis represents the along-shore component (units: N/m^2).

We can see that on the first two days there is a maximum in wind intensity with values around -0.05 N/m^2 and, followed by a weakening of the wind field until day 4 (second red arrow) with a minimum of -0.02 N/m^2. On the 5th of September, the along-shore component intensified, again, with values of -0.09 N/m^2. Between the 6th and 9th of September, there is a decrease in wind intensity to values of -0.03 N/m^2. However, the maximum along-shore component is reached on days 10 and 11 with values of -0.16 N/m^2. From day 11 onwards, wind stress decreases in intensity until it reaches zero values between days 16 and 20.

3.2.2   SST and Chl-*a* Patterns

Here we present the images of the sea surface temperature in response to the wind forcing. The SST images sequences for the first half of September is presented in figure 3.5.
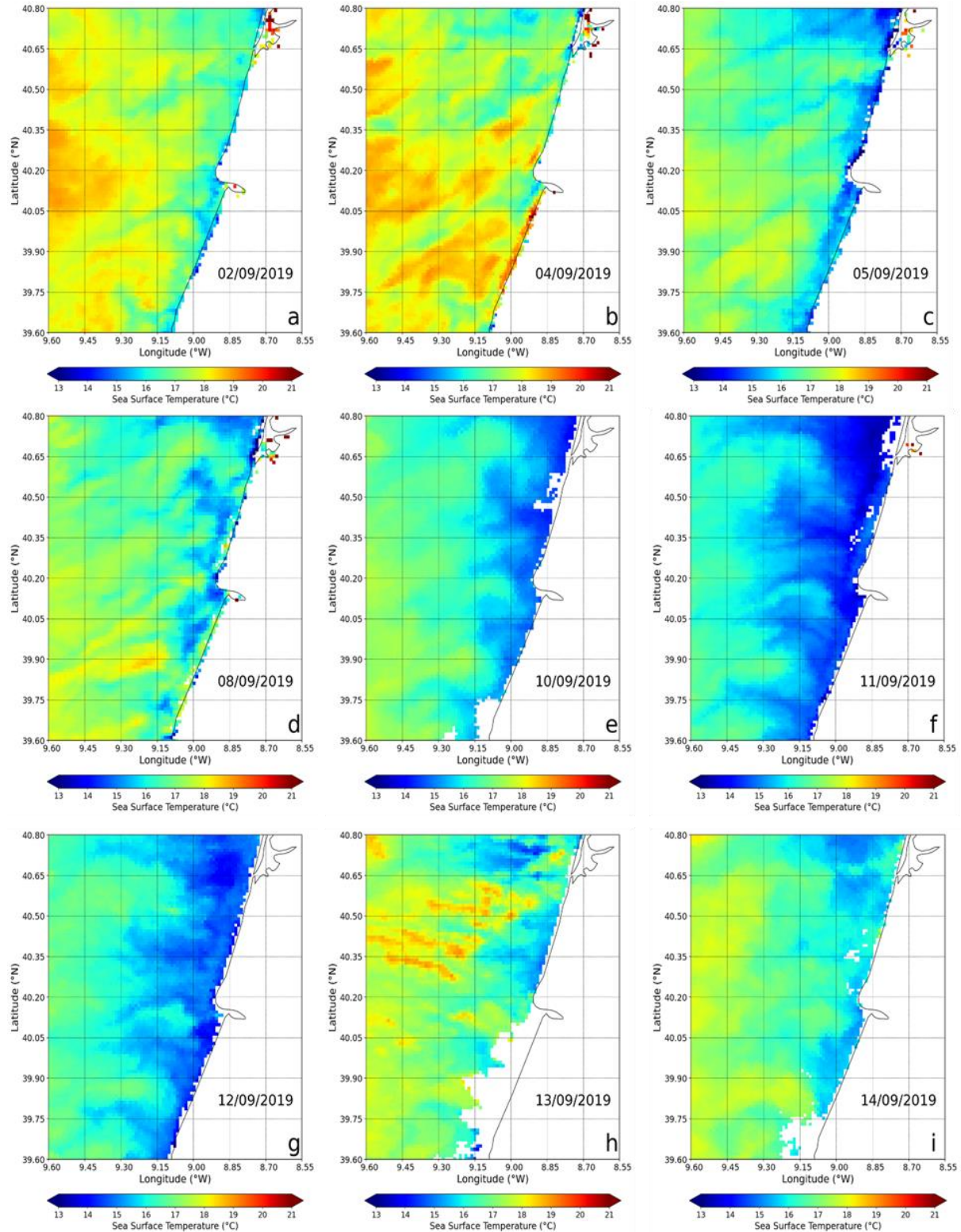
Figure 3.5: Spatial and temporal representation of sea surface temperature using SLSTR data for September 2019. The first row of images is for the 2nd, 4th, and 5th of September (images a, b, and c). The second line is the 8th, 10th, and 11th of September

(images d, e, and f). The third line of images is the 12th, 13th, and 14th of September (images g, h, and i). The white pixels represent the clouds and Portuguese territory

In Fig. 3.5a, 2nd September, we can see a thermal gradient from offshore to the coastal region and the presence of filamentous patterns, with temperatures between 17.0°C and 16.0°C. The coldest waters are located throughout the coastal band with temperatures between 16.0°C and 14.0°C. In the regions (9.60°W and 9.30°W) there is a gradual increase in temperature with the highest values between 19.0°C and 18.0°C.

On the 4th, image b, there is general warming of the ocean with temperatures between 18.0°C and 19.0°C. However, the region below Cape Mondego (40.20°N and 39.75°N) presents higher with values above 18.0°C, while the coastal strip of 40.20°N and 40.80°N has temperatures below 16.0°C.

Between the 8th and 10th, there is a reappearance of cooler waters with temperatures below 15.0°C and a spatial progression of cold waters to the sea. During this period, it is possible to observe several well-defined filamentous patterns that extend from the coast to the offshore, around 9.45°W.

In image f, the 11th, it is observed that the sea surface reached the lowest temperatures with values below 14.0°C in the entire coastal strip, and in certain regions, they extend to 9.60°W through the filaments.

From the 12th to the 14th, there is a progressive increase in sea surface temperature to values between 15.0°C and 16.0°C, thus being confined to coastal regions (9.15°W). Consequently, from the decrease in the sea surface temperature, it is possible to notice, again, a thermal gradient in the last two days (13th and 14th).

The satellite-derived Chl-*a* concentration image sequence, for the same dates as for the SST images, is shown in figure 3.6.
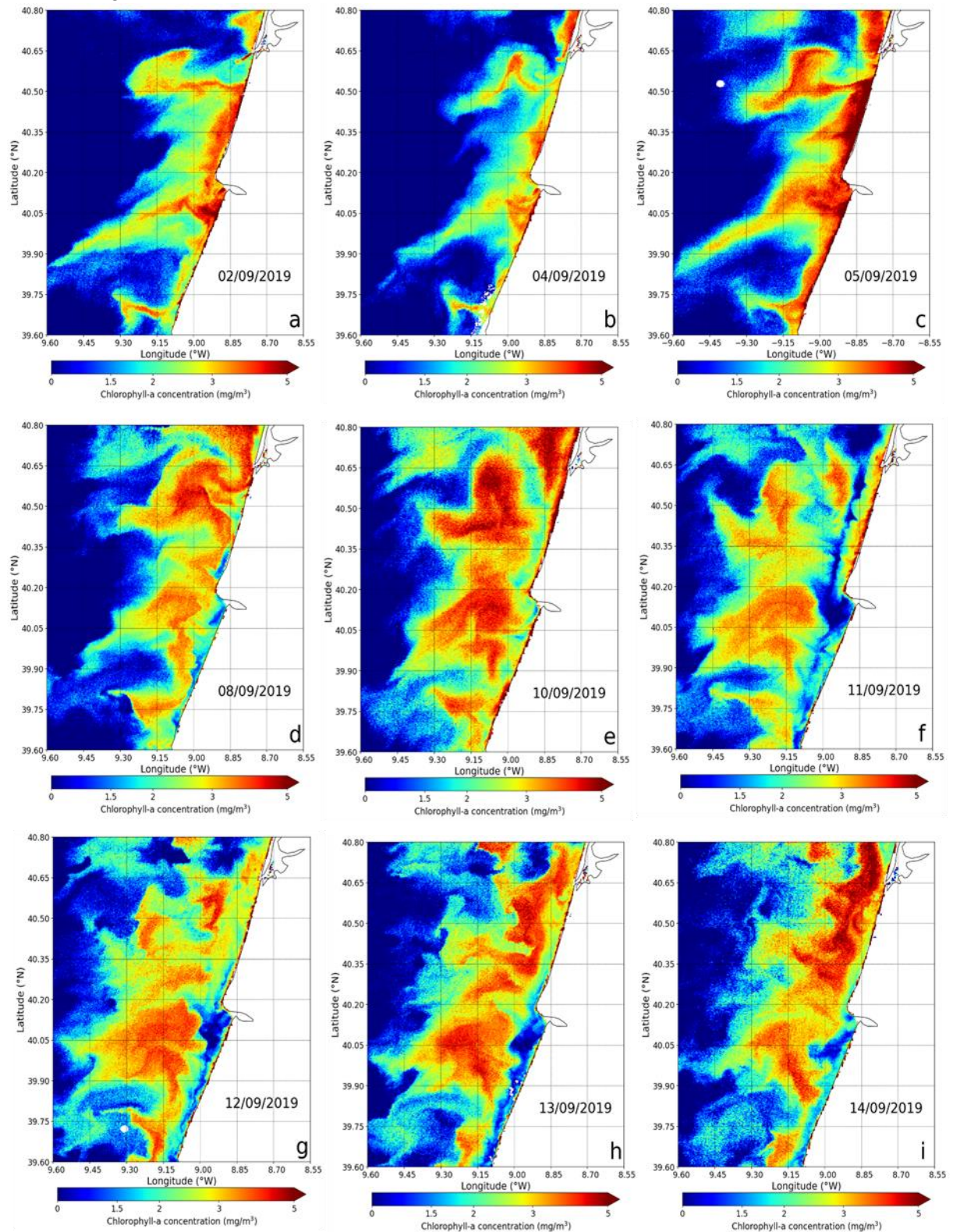
Figure 3.6: Spatial and temporal representation of coastal upwelling patterns using Piscismod Iberia data for the first 15 days of September 2019. Images a, b and c are the 2nd, 4th, and 5th of September 2019. Images d, e, and f are the days 8th, 10th, and 11th of September. Images g, h and i are the 12th, 13th, and 14th of September. The white pixels represent the clouds and Portuguese territory.

From the 2nd of September, it is possible to observe a filament of high values of *Chl-a* extending from the coast out to 9.6°W. The highest concentrations of chlorophyll-*a* with values greater than 3 mg/m^3 are located along the coast between 40.00°N and 40.40°N.

Between the 2nd and 5th of September, there is an increase in the concentration of Chl-*a* at all latitudes (39.60°N and 40.80°N) offshore (8.85°W and 9.3°W), with values greater than 5 mg/m^3 on different areas.

On 5th, we can see an intensification in the concentrations of Chl-*a* with values above 3 mg/m^3 covering larger areas, specifically between 40.35°N and 40.65°N. Between the 8th and 10th, it is observed the disappearance of the defined shape of the filament, associated with the intensification of the wind.

On 8th, a sharp decrease in small chlorophyll-*a* is observed along the coast between 40.35°N and 39.65°N, with values below 1.5 mg/m^3. However, on 10th shows high concentrations of Chl-*a* along the coastal strip with values above 3 mg/m^3. Also, we observed at higher latitudes (40.20°N and 40.80°N) the separation between chlorophyll-*a* in the coastal region and offshore (lower concentration range of Chl-*a*).

On 11th, shows an alongshore strip, roughly between 9.00°W and 8.90°W with the low Chl-*a* concentrations that separates the phytoplankton biomass between the coastal (longitudes > 8.90°W) and offshore regions (longitudes < 9.00°W). For this day, the higher latitudes (40.20°N and 40.80°N) have higher concentrations of chlorophyll-*a* with values at 5 mg/m^3 compared to the ocean region with concentrations around 3 mg/m^3.

On the remaining days, the separation between the phytoplankton biomass observed on 11th of September, only exists between 39.60°N and 40.20°N, while in the higher latitudes (40.20°N and 40.80°N) there is no abrupt change in Chl-*a* concentrations. Although, an intensification of chlorophyll-*a* concentrations is observed in the northernmost regions of Cape Mondego (40.20°N) during this period.

3.2.3 Model ROMS
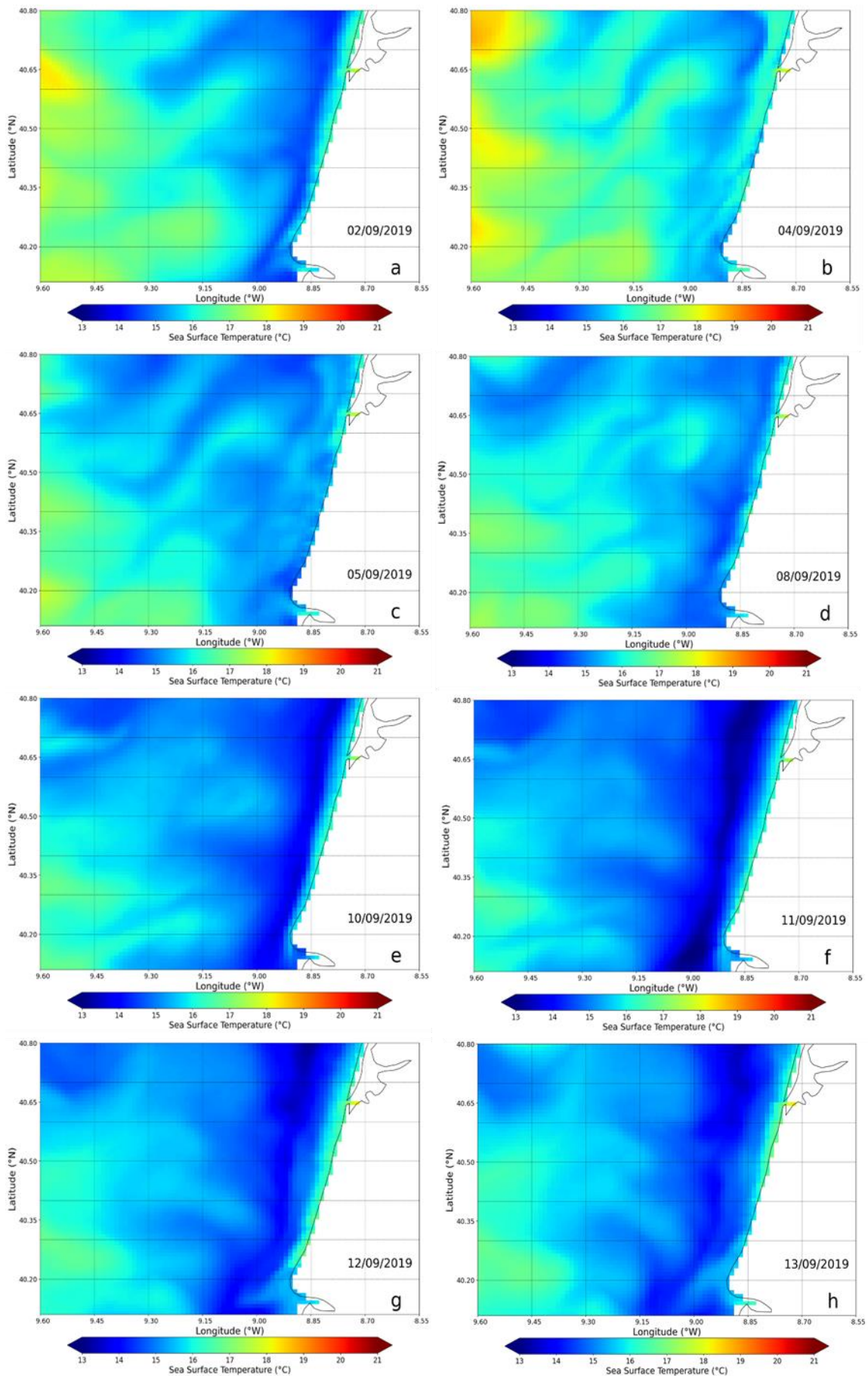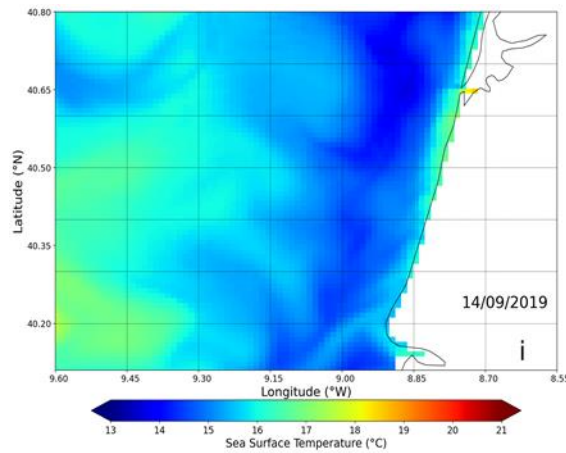
Figure 3.7: Spatial and temporal representation of sea surface temperature using numerical solution (ROMS) for September 2019. The images are displayed sequentially from the 2nd to the 14th of September

In figure 3.7, we can see how the numerical solution of the model represents the sea surface temperature for the first 15 days of September 2019. On 2nd, the model sea surface temperature varies between 15.0°C and 14.0 °C in coastal regions. A narrow coastal strip (longitude > 8.90°W) with temperatures 17°C higher than further offshore is present throughout the represented period between 40.35°N and 40.80°N (with a possible exception on day 5).

On 4th, there is a general decrease in sea temperature across the region. Above Cape Mondego we can observed an increase of the sea surface temperature compared to 2nd. It is also possible to observe the thermal gradient between the offshore and the coast.

On 5th and 8th, there is a decrease in sea surface temperature in the whole area, and with the cooler waters to the north (40.50°N and 40.80°N). Between 10th and 11th show the biggest decrease of all days with the appearance of a temperature range with values below 13.0°C, running parallel to the coastal strip between 9.00°W and 8.90°W. However, these temperatures are more accentuated during September 11, 2019.

On the remaining days, there is a progression of warmer temperatures (16.0°C) to 9.30°W and a spatial decrease of the low-temperature range to the northern latitudes (40.60°N and 40.80°N).

3.2.4　Cross-shore variability

To further characterize the cross-shore variability a latitudinal average between 40.35 °N and 40.40 °N was performed in a longitudinal section, to study the spatial evolution of the sea surface temperature and the concentration of chlorophyll-*a*.
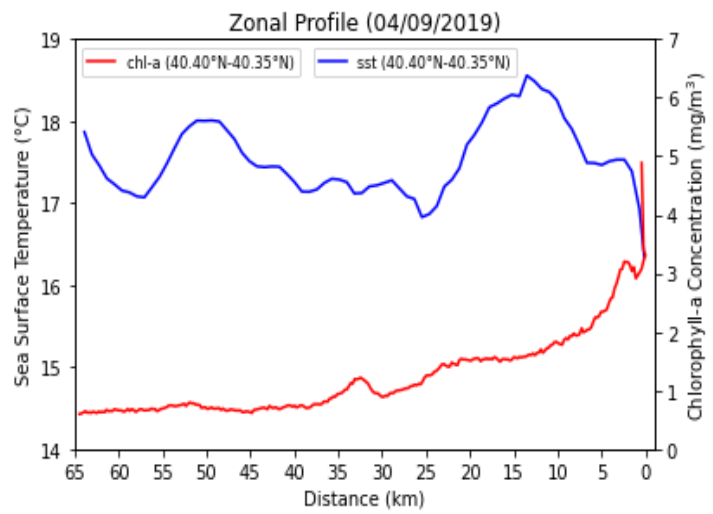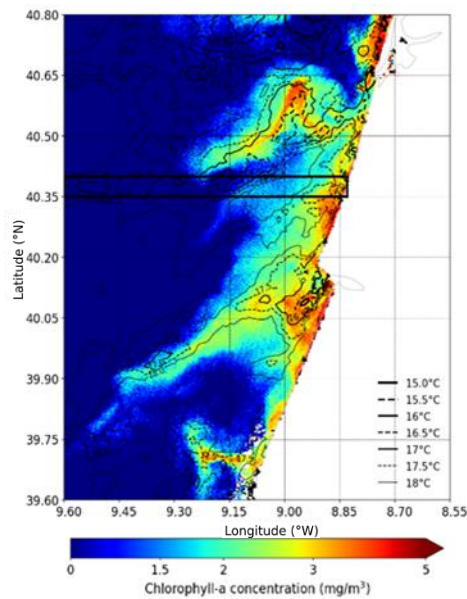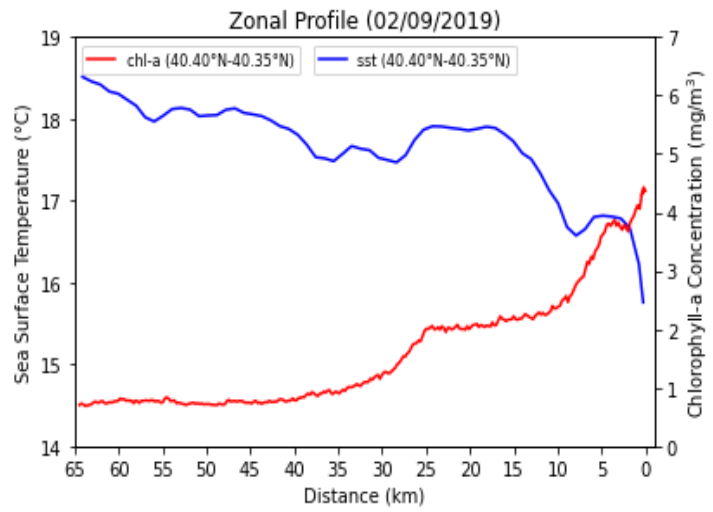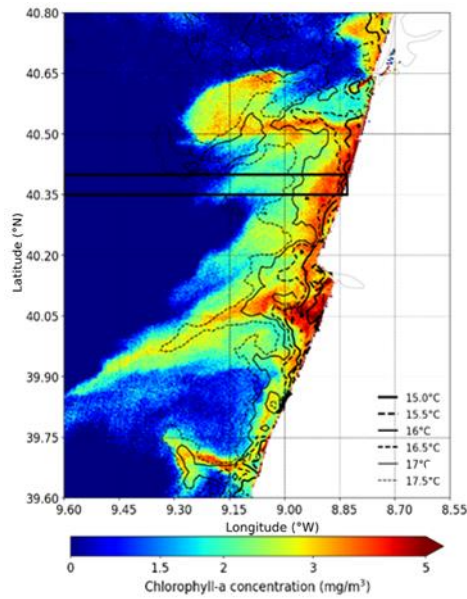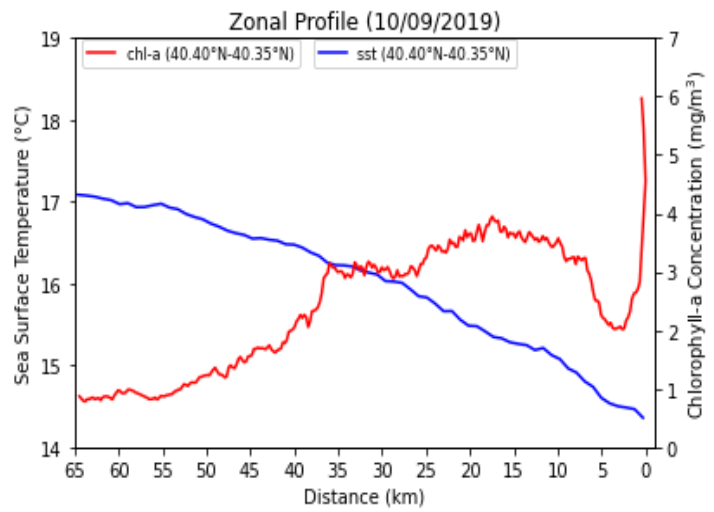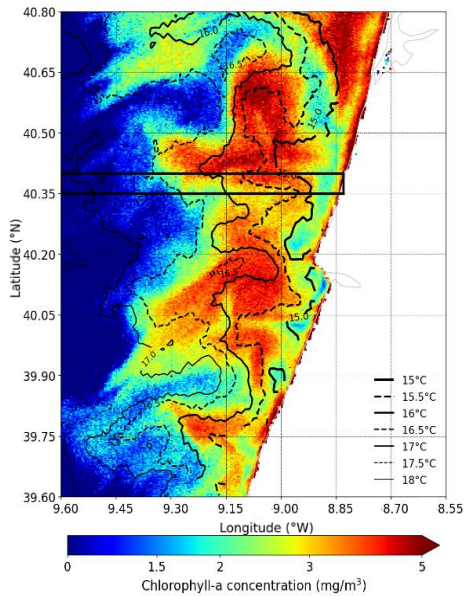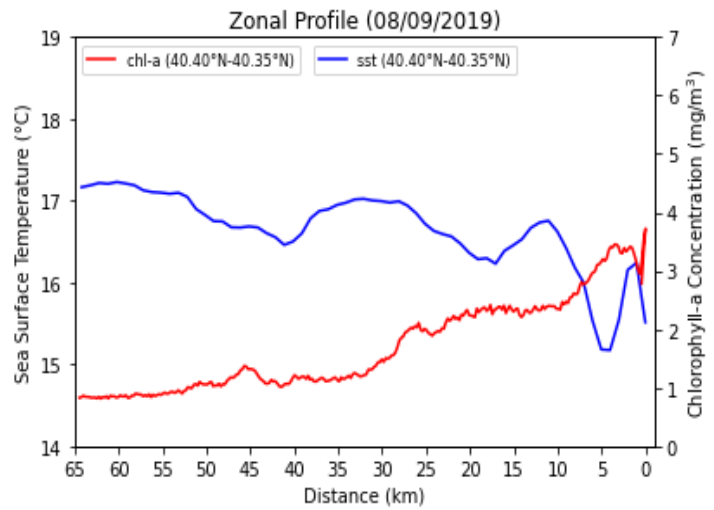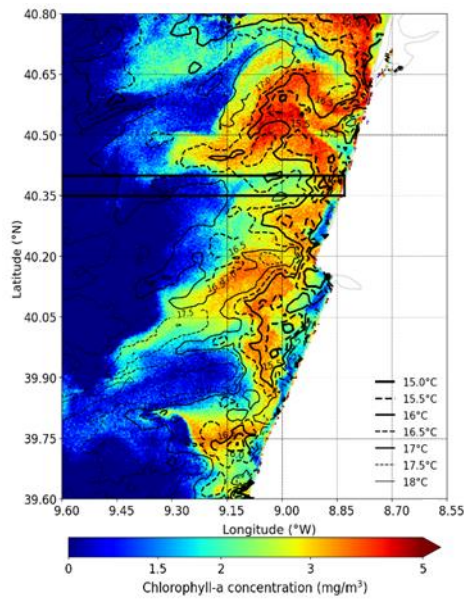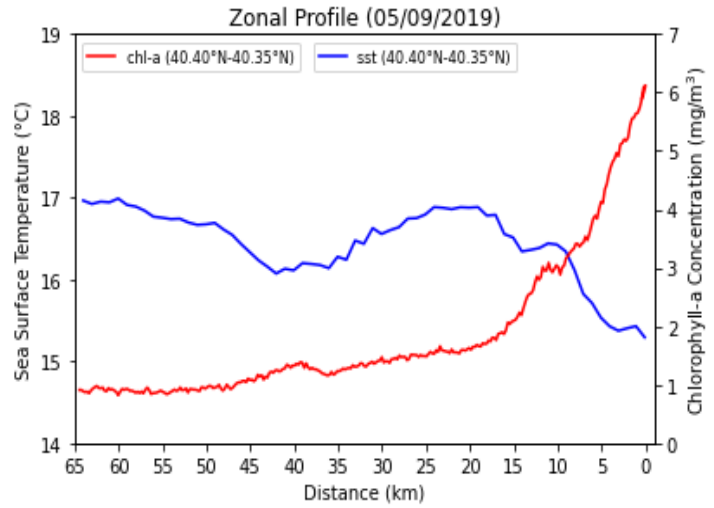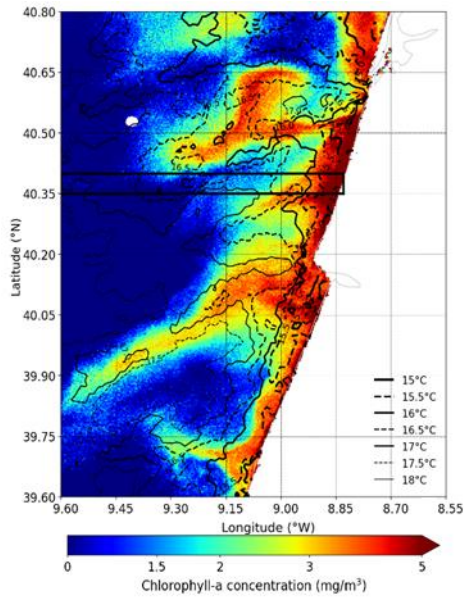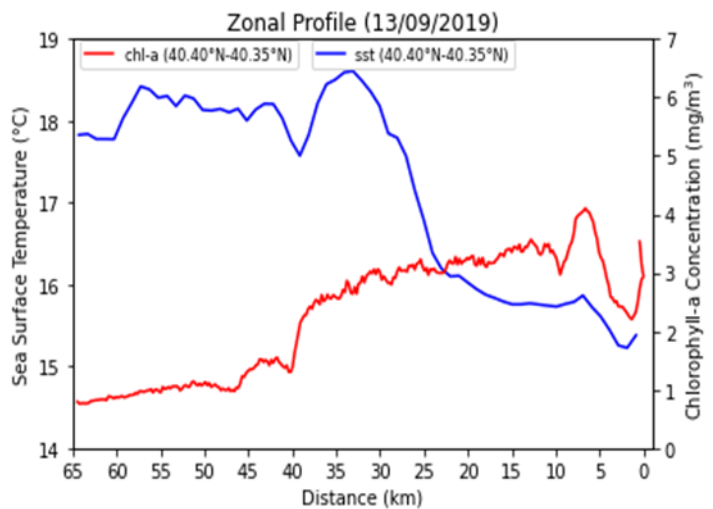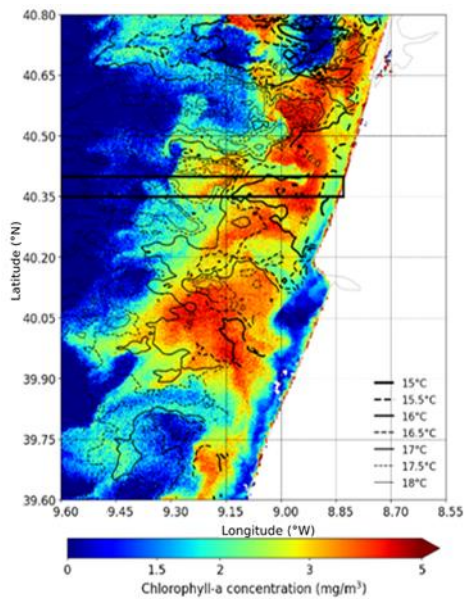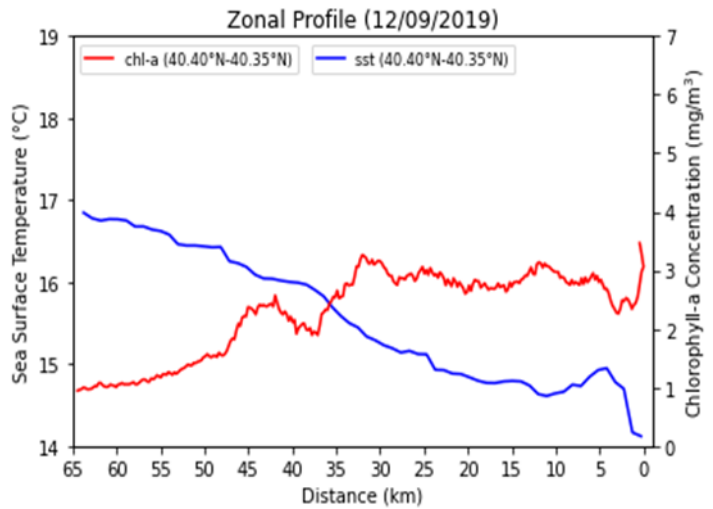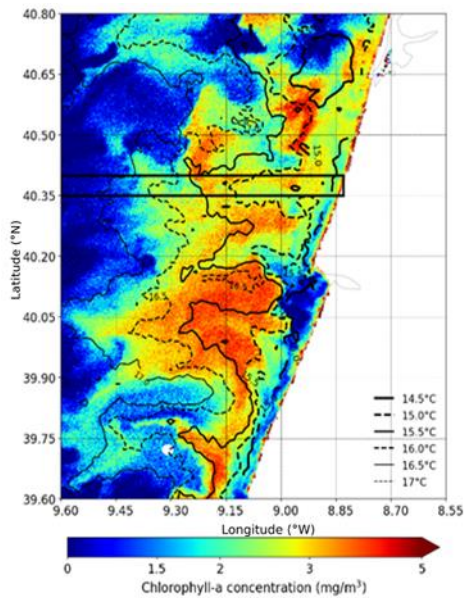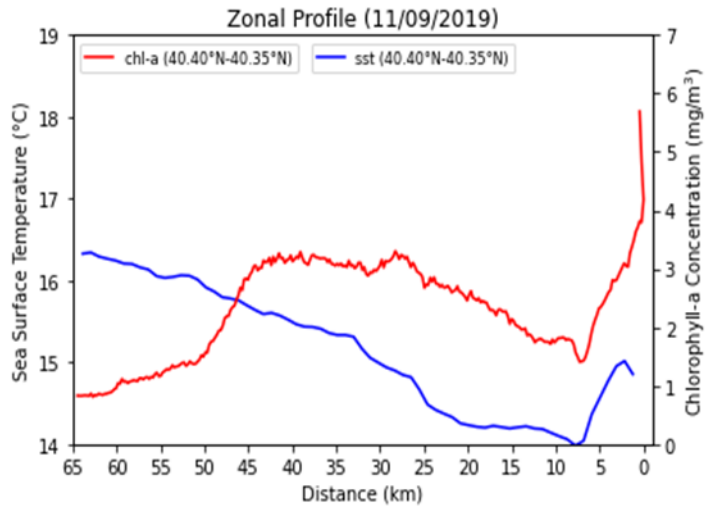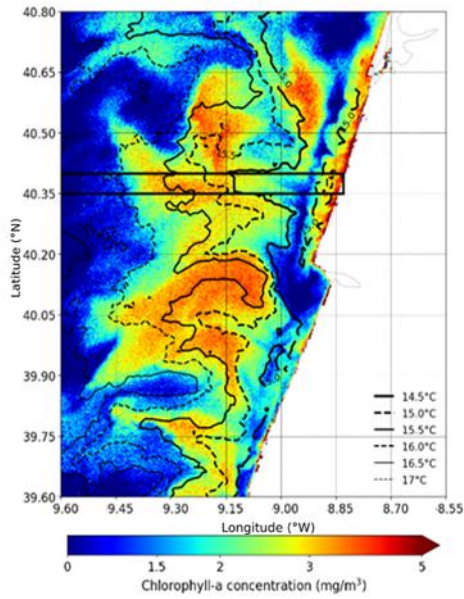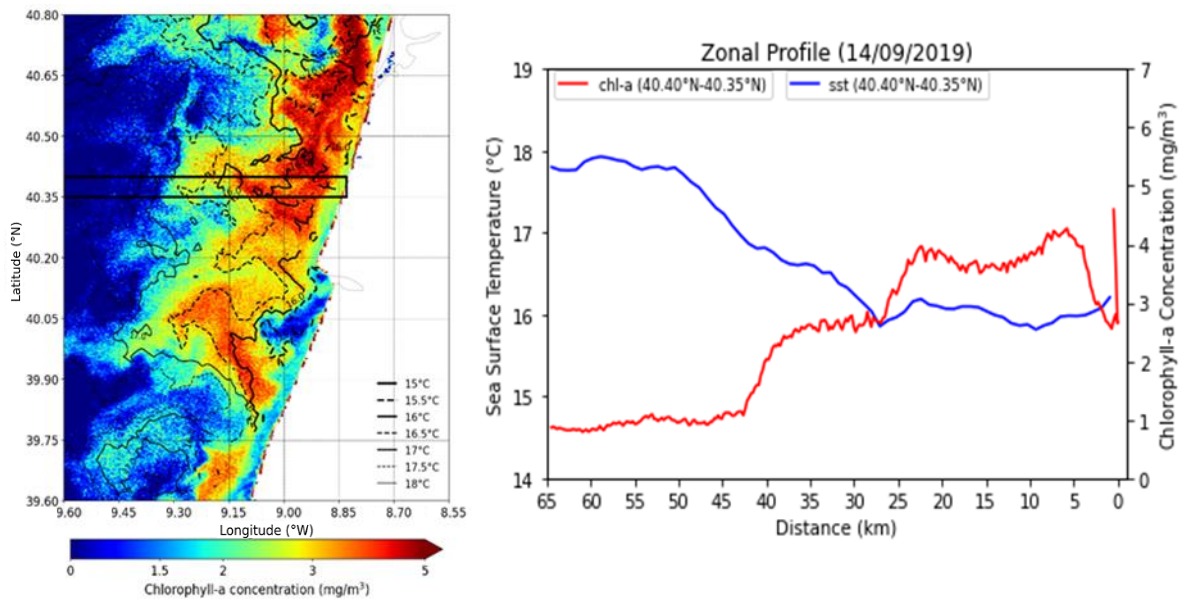
Figure 3.8: Spatial and temporal representation of coastal outcrop patterns with isothermal lines (left images) and quantitative analysis of chlorophyll-*a* concentration (red line) and sea surface temperature (blue line) based on a latitudinal mean along a longitudinal transect (right images) for the first 15 days of September 2019. The black rectangle represents the area where the mean was applied. Isothermal lines are separated by 0.5°C. The x-axis showed in the zonal profile represents the distance to the coast.

The images on the left show that the concentration of chlorophyll-*a* generally follow the isothermal lines, that is, the phytoplanktonic biomass tends to follow the cooler waters, however, this relationship changes at different stages of wind forcing.

On the 2nd of September, it is observed that offshore between 65 km and 30 km the sea surface temperature decreases coastward from 18.5°C to 17.8°C. However, the concentration of Chl-*a*, in the same longitudes, presents values lower than 2 mg/m^3. Only from 25 km of the coast does the phytoplanktonic biomass start to increase until it reaches its maximum on the coast with values above 4 mg/m^3. This increase in the amount of phytoplankton occurred when the sea surface was below 17°C.

On day 4, the SST shows large spatial variability with values between 17.0°C and 18.0°C, offshore. The Chl-*a* concentration exhibits a behaviour similar to that on day 2 with values below 2 mg/m^3. From 25 km of the coast, the temperature increases again until reaching a maximum of 18.6°C, at 10 km off the coast, before decreasing again to values below 17.0°C. At the same time, there is a slow increase in phytoplankton biomass, during the maximum temperature, with values of 2 mg/m^3. From 5 km to the coast, there is a marked increase in the concentration of chlorophyll-*a* with a maximum of 4.9 mg/m^2, associated with a decrease in water temperature.

On 5th and 8th, the cross-shore SST and Chl-*a* profiles show a similar behavior of decrease/increase SST/Chl-*a* as it approaches the coastal region. On day 5, SST remains approximately constant offshore to 10 km and then drops to values below 16.0°C towards the coast. On this day there is a chlorophyll-*a* increase between 10 km and the coast, with a maximum of 6 mg/m^3.

On the 10th of September, there is a more pronounced decrease/increase in offshore SST/Chl-*a* when compared to the previous days. On the previous days, the intensification of chlorophyll-*a* concentration occurred in coastal regions (10 km from the coast), but on the 10th of September there is a Chl-*a* increase, with values above 2 mg/m^3, at 35 km to the coast. Between 35 km and 10 km, there is a rise in chlorophyll-*a* with a maximum of 3.8 mg/m^3 before declining abruptly to a minimum of 2.0 mg/m^3

around 5 km. Then, we again observed an increase in the amount of chlorophyll-*a* with a peak of 6 mg/m^3 in the more coastal zone.

On day 11, the temperature of the sea surface has a similar decrease as on day 10, however in the coastal region the temperature increases again. Chlorophyll-*a* concentrations increase in quantity, around 45 km, with values between 2 mg/m^3 and 3 mg/m^3. Between 35 km and 5 km, there is a decrease in chlorophyll with a minimum of 1.6 mg/m^3 (the lowest Chl-*a* concentration of all the days) before it increases again towards the coastal region with values above 5 mg/m^3.

On the 12th of September presents a constant decrease in sea surface temperature from offshore to the coastal region, i.e., the temperature decreases from 16.9°C to 14.2°C. The chlorophyll concentration increases from 30 km to the coast, until it reaches a value higher than 3 mg/m^3 near the coastal region.

On the 13th of September presents a temperature with little variability offshore until 30 km, with values ranging between 18.8°C and 19.6°C. From 30 km to the coast, the temperature drops sharply with values below 16.0°C. The phytoplankton biomass shows a behavior identical to the previous days, with an increase in concentration as it approaches the coast. However, it has a marked decrease between 5 km and 3 km, with values below 3 mg/m^3.

The 14th of September shows a decrease in temperature from offshore to the coast, like the other days. Phytoplankton, too, shows a behavior identical to the other days, such as the 13th.

3.2.4.1   Relationship between SST and Chl-*a* with model fields:

In this section we analyse in greater detail the satellite images and the model solutions for the 5th, 10th, and 11th of September 2019, as they correspond to the days of stronger wind forcing (Fig. 3.4). Three different latitudes (40.30°N, 40.19°N, and 40.11°N) were selected to represent how ocean currents and temperature vary with depth. The representation of the model currents and temperature were produced. These were combined with satellite-derived distributions to provide a "3D" perspective. The models solutions indicated that mixed layer off the Portuguese coast, in September, has a depth of between 20 and 30 meters in accordance with De Boyer Montégut et al. (2004). Thus, all representations with ocean currents were made with integration between 0 to 20 meters.

3.2.4.2   5th of September

For September 5, 2019, the representations of chlorophyll-*a* concentration, sea surface temperature, and horizontal divergence with ocean currents (integrated for the first 20 meters) are presented in Fig. 3.9. To explore the relationship between phytoplankton biomass in the mixed layer and the physical variables from the ocean model.
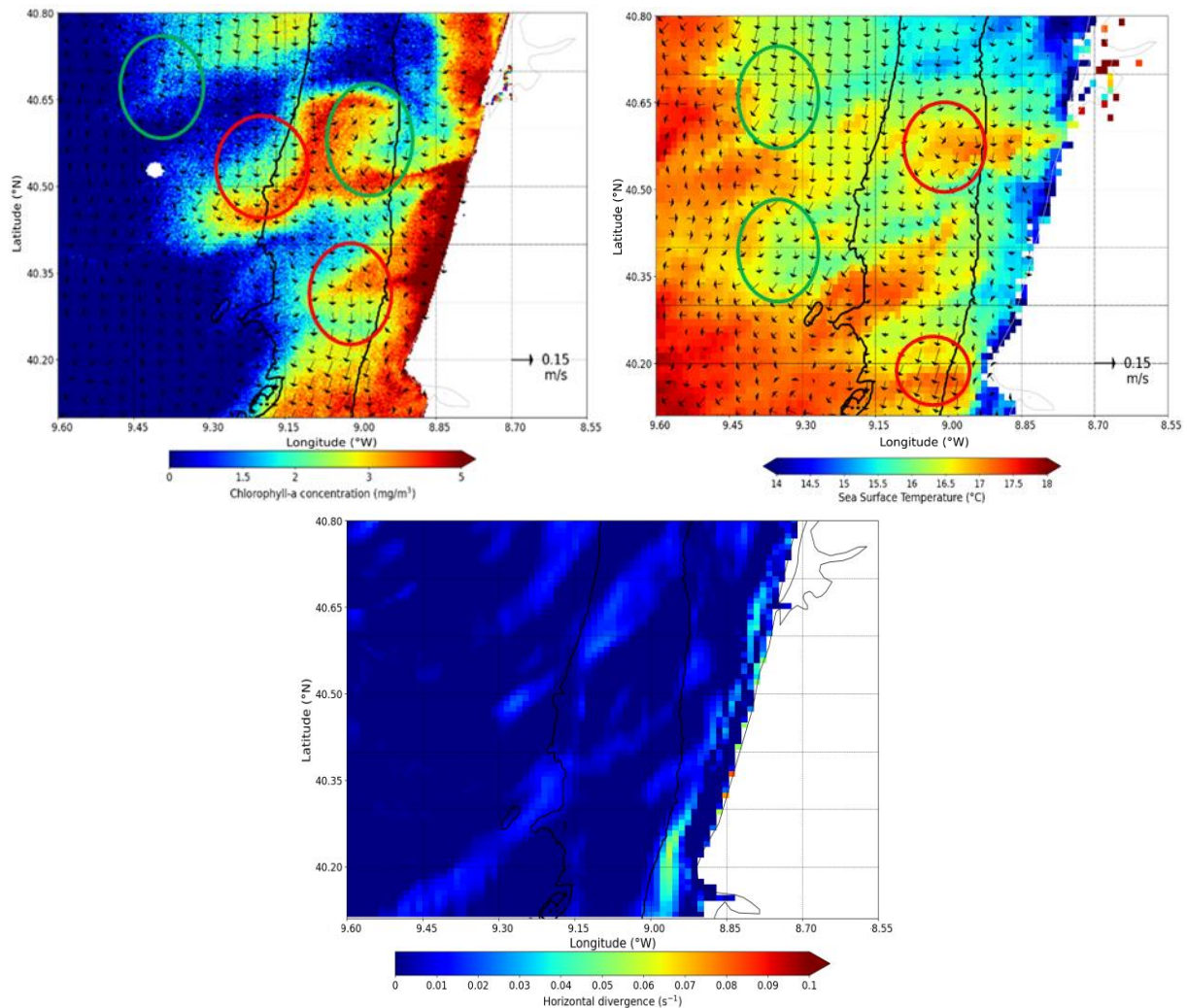
Figure 3.9: The image on the left is the concentration of chlorophyll-*a* and the image on the right is the sea surface temperature, with the black arrows corresponding to the average of ocean currents in the first 20 meters of the water column. The bottom image is the horizontal divergence for the 5th of September of 2019. The red circles represent a poor visual agreement between

the model solutions and the spatial distribution of the phenomenon. The green circles represent a good visual agreement between the model solutions and the spatial distribution of the phenomenon.

The figure shows that the distribution of concentrations of chlorophyll-*a* are similar to ocean currents in some regions, however, in other places, the same is not observed. For example, in the case of the marked with the green circles (40.80°N:40.65°N, 9.45°W:9.30°W; 40.65°W:40.50°W, 9.13°W:8.90°W), the phytoplankton biomass appears to be moving in the same direction as the ocean currents.

In the areas marked with the red circles, the phytoplankton biomass does not exhibit the expected pattern of a passive tracer being transported by the ocean currents. Similarly, in the image on the left, we can see that the spatial distribution of sea surface temperature has a behaviour analogous to ocean currents in certain regions (green circles), and in other places, they differ from each other (red circles). In the green circles, the SST field tends to follow the direction of ocean currents (isotherms are parallel to currents vectors), contrary to the areas marked with the red circles.

The horizontal divergence field show that the regions with the highest values are found along the Mondego Cape (latitudes: 40.30°N and 40.11°N and longitudes: 9.00°W and 8.94°W) with values around 0.04 s^{-1} and 0.06 s^{-1}, and below the Aveiro estuary (latitudes: 40.70°N and 40.55°N and longitudes: 8.85°W and 8.80°W) with values of 0.04 s^{-1}. In the rest of the image, the field of horizontal divergence is practically nil, except in some regions where values oscillate between 0.01 s^{-1} and 0.03 s^{-1}.
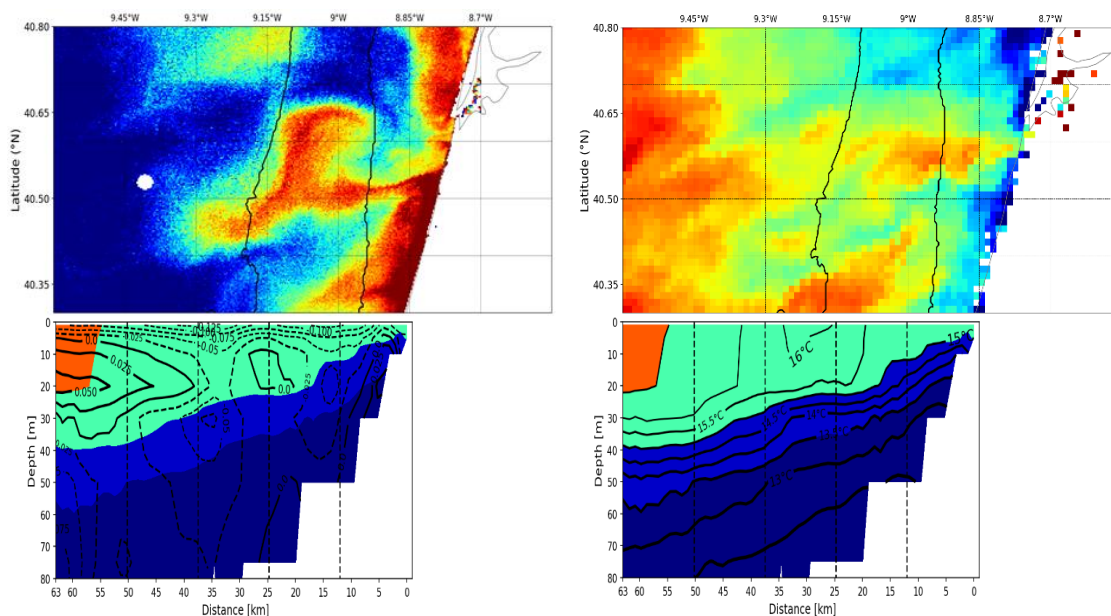
Figure 3.10: The image in the upper left corner is the concentration of chlorophyll-*a*, with the image in the lower-left corner representing ocean current velocities at depth for latitude 40.30°N (southern limit of the Chl-*a* image). Bold lines in the vertical profile represent northerly currents, dashed lines represent southerly currents, and colours represent sea temperature. In the upper right corner is the sea surface temperature. The bottom right image is the sea temperature at depth with the isothermal lines plotted at 0.5°C intervals for the latitude 40.30°N. Bold lines represent cooler water layers and dashed lines represent warmer water bodies.

In general, for the 5th of September, the ocean currents are predominantly to the south, except for the coastal region and the offshore region. We can observe, from the coast to the sea, between the first 5 meters, the currents present a southerly direction with the highest speeds near the surface (-0.125 m/s) due to the presence of the wind. However, the velocity of the currents tends to decrease with depth with values of -0.025 m/s, at 5 meters. Between the offshore limit and 9.30°W with a depth of around 5 and 35 meters, there is an inversion in the direction of the current (northern direction), with a dimension of

approximately 26 km. The strongest currents are found at a depth of 20 meters with a value of 0.050 m/s, over the offshore limit. In the coastal region (between the 20 km and 5 km), we find that the first 3 meters are dominated by southward currents, with speeds between -0.075 m/s and -0.100 m/s, and with a cross-shore extension of 2 km. However, from 3 meters to 30 meters there is an 8 km wide current with a northward direction with a speed of 0.025 m/s. In the image on the left, we observe the same water bodies at different depths depending on whether they are in the oceanic region or the coastal region. As an example, the water with a temperature of 15°C was 40 meters deep in the oceanic region (9.60°W) and as it approaches the coast it presents a sharp decrease in depth up to 6 meters. This behaviour can be seen throughout the water column. We can also verify that water masses with temperatures between 15°C and 13.5°C exhibit a more accentuated temperature cooling at depth due to the proximity of isothermal lines concerning water masses with values between 13.5°C and 12.5°C.

Next, we do the identical plot for the latitudes 40.19°N and 40.11°N to see how ocean currents and temperature vary in depth and latitude.
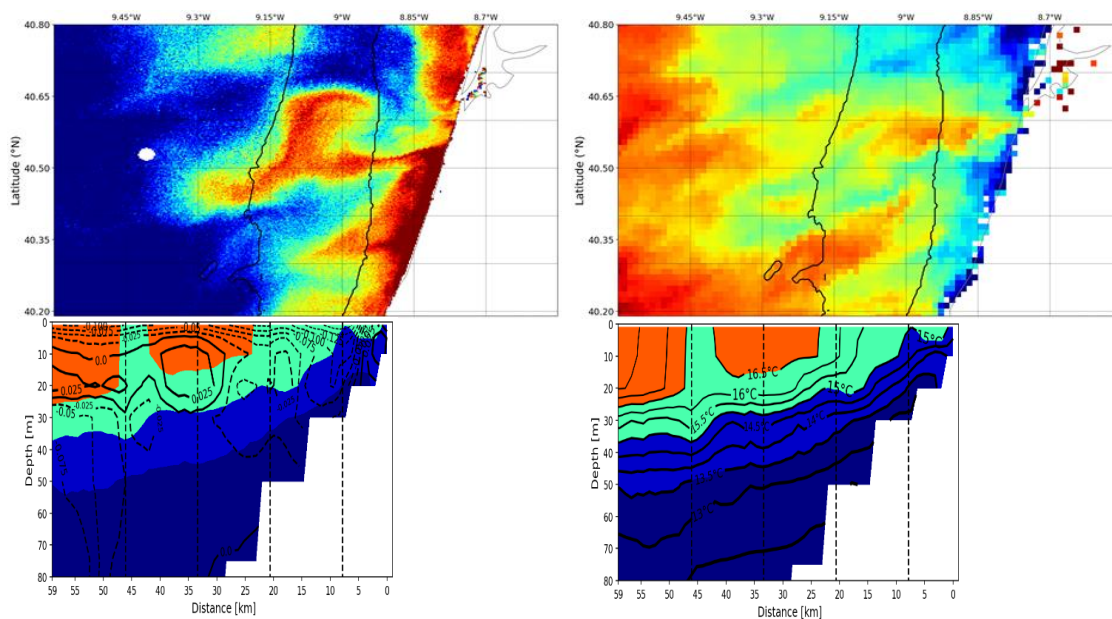
Figure 3.11: Same as Fig. 3.10 but for the latitude interval 40.80°N-40.19°N and cross-shore sections at 40.19°N.

At the latitude of 40.19°N, we observe that ocean currents continue in a southerly direction at a depth of 7 meters between the longitudes of 9.60°W and 9.20°W. However, between 9.20°W and 8.90°W, currents reach a maximum depth of 50 meters. Currents with the highest speeds are found near the coastal region (7 km off the coast and at a depth of 15 m) with a maximum of -0.150 m/s. We can see that the region with the highest speeds recorded is located between 7 km and 5 km off the coast. Between 5 km and the coast, there is a current with a northerly direction with a speed of 0.025 m/s. It is still possible to notice two southward branches with speeds of 0.025 m/s, one is located at about 9.60°W, and the other at 9.30°W, both have the same depth approximately. In the sea temperature section, it is observed a behaviour similar to the latitude of 40.30°N. At a longitude of 9.45°W, we find that a mass of water with a temperature of 16.5°C reaches the surface separating the colder coastal waters from the warmer water offshore.
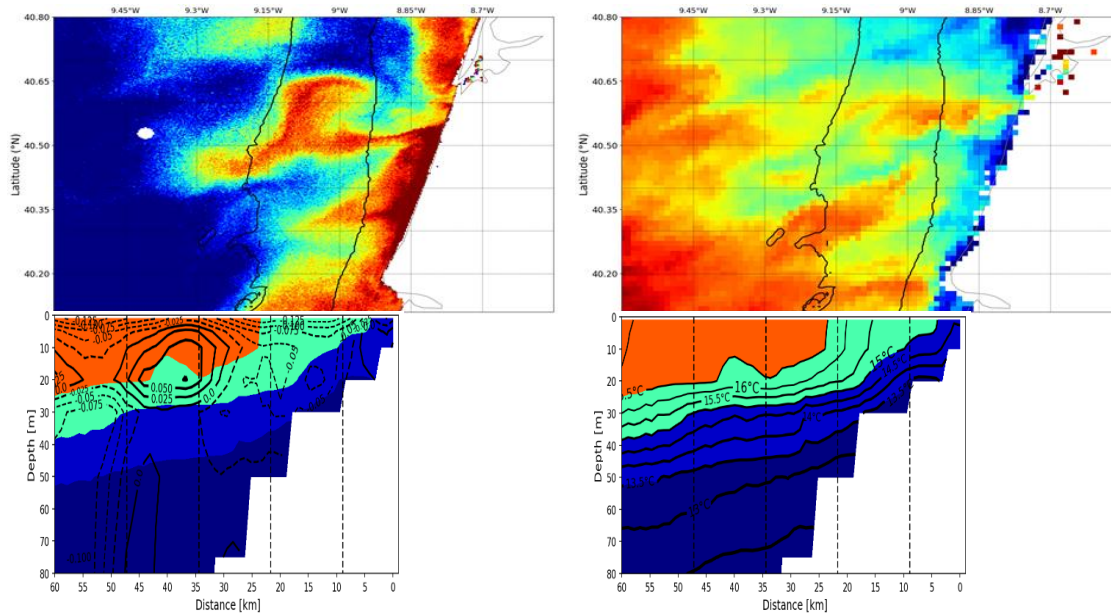
Figure 3.12: Same as Fig. 3.11 but for the latitude interval 40.80°N-40.11°N and cross-shore sections at 40.11°N

At 40.11°N (South of Cape Mondego), ocean currents present the same southward orientation at the surface, such as the previous latitudes. The depth of these currents varies along the longitude, that is, between 9.60°W and 9.30°W the depth varies between 10 meters and 3 meters, and, later, the depth increases again until reaching a maximum of 50 meters. The northward currents are located at the same lengths and depths as the previous latitude (40.19°N); however, they have a higher velocity with a value of 0.050 m/s and a dimension of approximately 13 km. In the coastal region, the highest velocity has a value of -0.050 m/s has the lowest velocity compared with the other two latitudes. Sea temperatures present the expected behaviour of water masses with lower temperatures emerging from the surface near the coast. In this case, we can see that there is an extension of 3 km of cold water (15°C) along the coast.
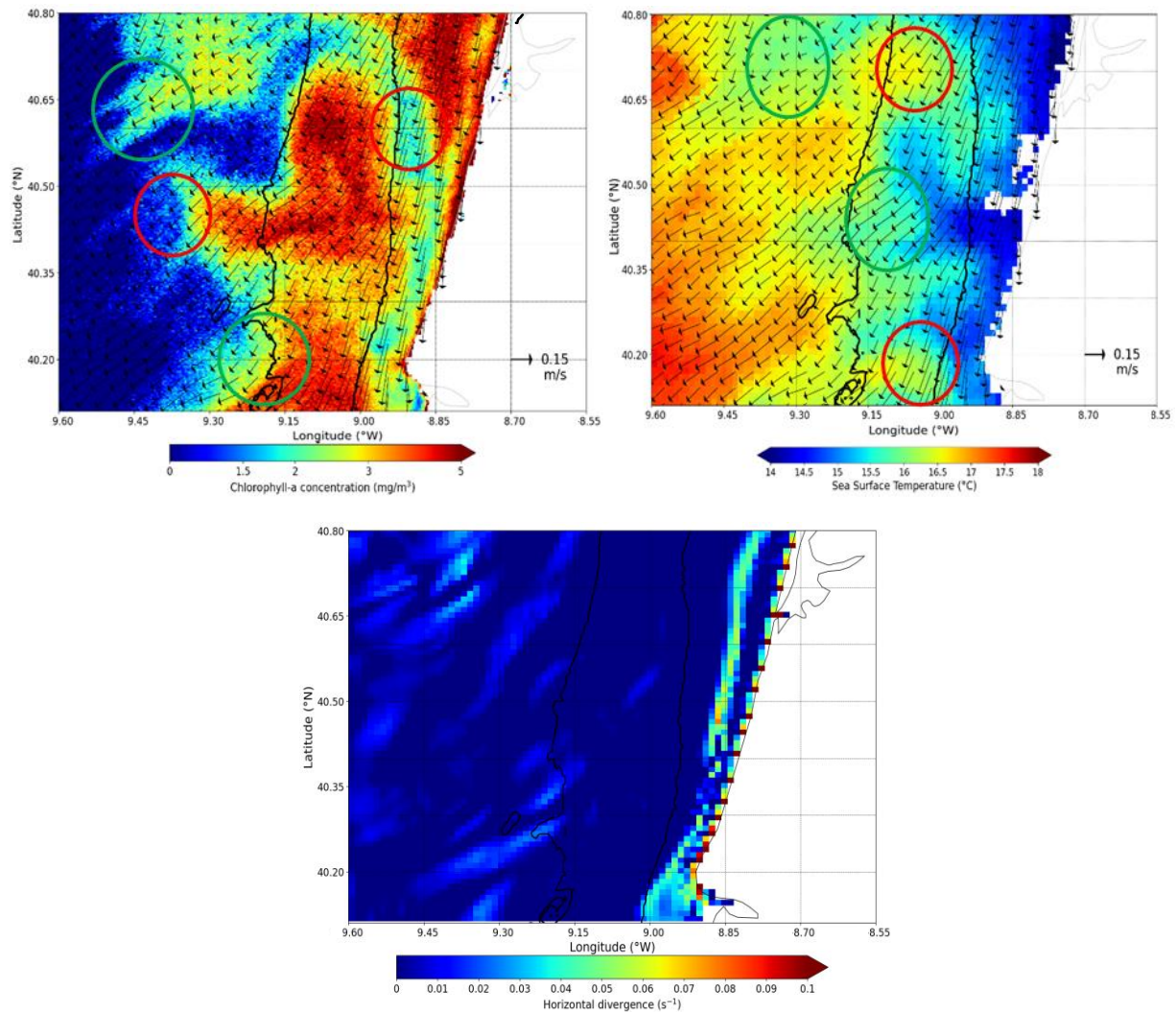
Figure 3.13: The same representation Fig. 3.9, but for the 10th of September.

We can notice that the spatial distribution of phytoplankton follows ocean currents, except in some places. In Chl-*a* and SST patterns there was a small change in the areas of agreement/disagreement compared to September 5th. For example, in the case of the area marked with the red circle near the 50 m isobath (for the Chl-*a* image) represents an area with low visual agreement between the model and the distributions while for the 5th of September was represented as a good visual agreement. Circles (red and green) located offshore remained similar.

In the case of SST, the areas of agreement and disagreement do not show a significant change from the 5th to the 10th, only the green circle (between 40.50°N and 40.35°N) that shifted to the middle of the 100 m and 50 m isobaths. The field of horizontal divergence increased in intensity and dimension compared to the previous day (day 5). Between 40.67°N and 40.55°N (green circle), phytoplankton has a spatial distribution in the southwest direction that corresponds to the direction represented in the currents. The second location, where we observe a spatial structure of the phytoplanktonic biomass coincident with the direction of the currents, is located near the 100 m isobath. One of the places, where there is no apparent connection between the spatial distribution of chlorophyll-*a* and ocean currents, is found near the 50 m isobath. In this red circle, we notice a zone of low concentration of chlorophyll-*a* that matches

with highest values of the horizontal divergence. Between 9.45°W and 9.30°W, we also register a spatial distribution of phytoplankton that does not coincide with the direction of ocean currents for the area.

For sea surface temperature, both green circles show a concordant spatial distribution between temperature and ocean currents. The places represented by the red circles exhibit high-intensity ocean currents, however we did not verify a spatial structure of the temperature associated with the water transport carried out by them. In the field of horizontal divergence, we can see that the oceanic region (9.60°W and 9.15°W) has the lowest speeds compared to the coastal region (9.00°W and 8.85°W). In the context of the coastal region, we find two bands of horizontal divergence that propagate parallel to the coastline and with different speeds. The divergence band coupled to shorelines presents the highest values from 0.07 s^{-1} to 0.1 s^{-1} in relation to the second band (more oceanic) with velocities between 0.04 s^{-1} and 0.06 s^{-1}.
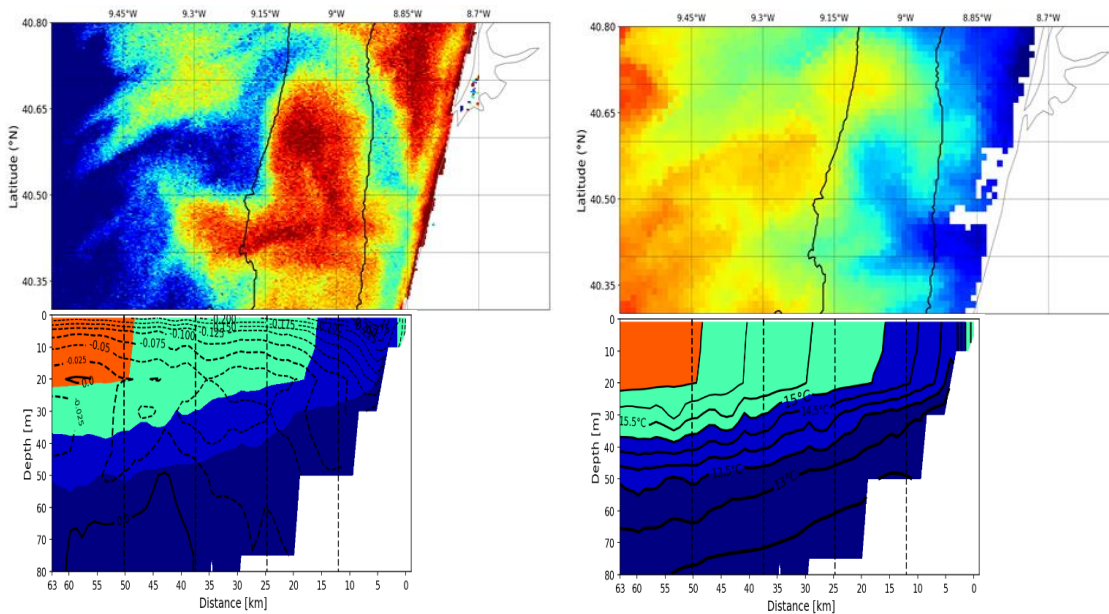
Figure 3.14: The same representation Fig. 3.10, but for the 10th of September.

For latitude 40.30°N, ocean currents are primarily southward with speeds increasing as depth decreases. The site with the most intense currents is located 10 km from the coast with a maximum of -0.275 m/s. The region with the highest velocities coincides with the area with the lowest concentrations of Chl-*a*. For the sea temperature, we observed a progressive decrease in-depth for all water bodies, however subsurface waters with temperatures between 15°C and 14°C show the sharpest decrease in depth. From 20 km off the coast, these water bodies move from a depth of 23 meters to the surface, in an extension of less than 10 km. Later, the water masses reach a spatial distribution of 16 km on the surface. We also verified the existence of a layer of water with temperatures above 15°C near the coastal strip (extension of 2 km) with a maximum depth of 10 meters. In this case, the temperature shows a change in observed structure compared to day 5 (same latitude). That is, the isotherms are intersecting the surface, between the 25 km to the coast, which is not observed on day 5. In the profile of ocean currents there was no significant change compared to the previous day studied.
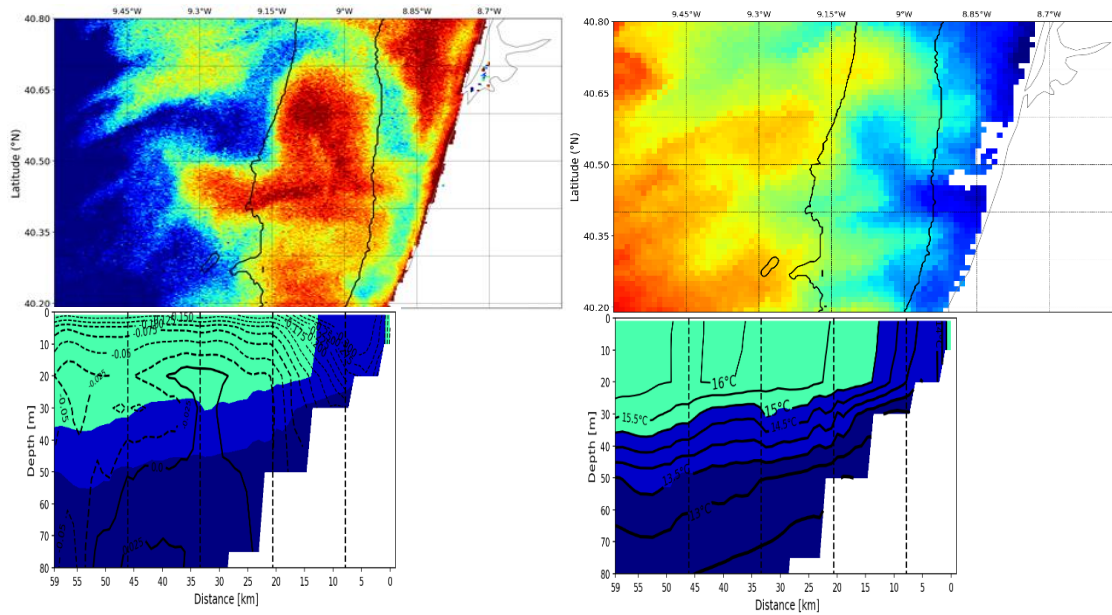
Figure 3.15: The same representation Fig. 3.11, but for the 10th of September.

For a latitude of 40.19°N, ocean currents continue southward throughout the water column except for the northward current at 70 meters deep. The highest currents are located on the surface with values of -0.150 m/s and the lowest currents with values of -0.025 m/s, from a depth of 17 meters. In the image on the left, the sea temperature has similar behavior to the latitude of 40.30°N, however, the colder water masses are closer to the coastal region in this case. In the profile of the ocean currents, it is possible to observe the formation of a coastal jet with a depth of 10 meters, 7 km off the coast. This structure is not visible for day 5 (same latitude). Also, the formation of this coastal jet coincides with the intersection of the isotherms with the surface.

Figure 3.16: The same representation Fig. 3.12, but for the 10th of September.

For latitude 40.11°N (South of Cape Mondego), ocean currents are mostly southward across the water column, except for a northward current where the water column is 60 m deep. The region with the most intense currents is at 9.00°W with a speed of -0.300 m/s at a depth of 4 meters. This region presents a

speed decrease to values of -0.175 m/s at a depth of 24 meters, however, this value of the ocean current is comparable to the values recorded at the surface, between 9.60°W and 9.45°W. Between 9.30°W and 9.15°W, we observed the existence of an abrupt variation in the speed of the currents due to the proximity of the dashed lines, in the first 10 meters of depth. In the image on the left, we can see the analogous behaviour for all studied latitudes, that is, the existence of colder water masses emerging close to the coast. These water masses compared to other latitudes are much larger (24 km) and show a variation in temperature patterns compared to day 5.

3.2.4.4   11th of September
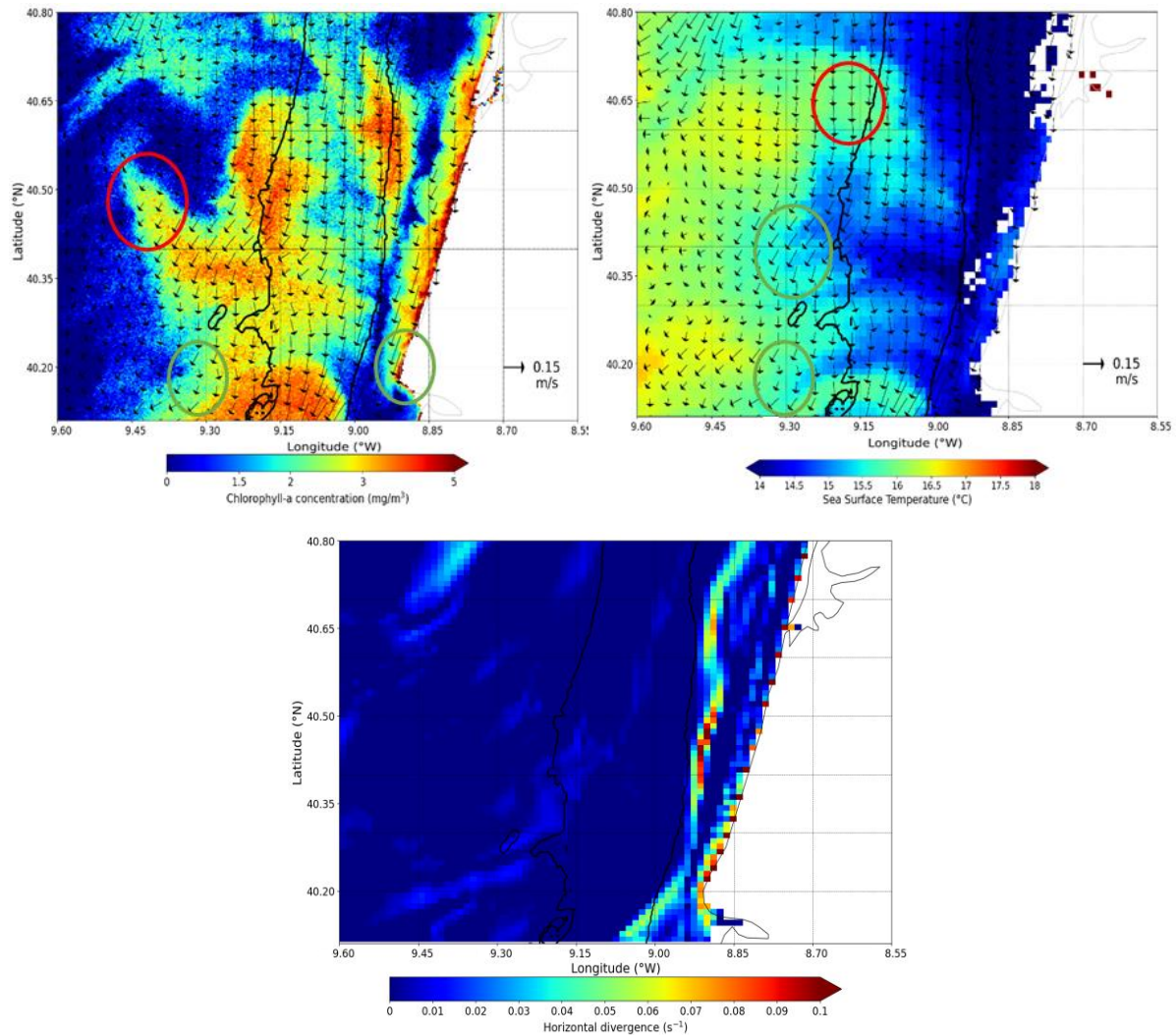
Figure 3.17: The same representation Fig. 3.9, but for the 11th of September.

In the Chl-*a* image, we observe that the spatial distribution of phytoplankton apparently influenced by ocean currents presents a behaviour identical to the previous days studied (September 5th and 10th). For September 11, the agreement/disagreement areas show some changes in positions (red and green circles) for Chl-*a* compared to previous days. As an example, near Cape Mondego it is possible to observe a good visual agreement between the model (green circle) and the distribution of Chl-*a* that did not exist in the previous days.

For SST, there are fewer areas with poor visual agreement compared to the previous days, while those marked with the green circle remain in the same places. One big difference is the intensification of the horizontal divergence in relation to the 5th of September. In the places represented with the green circles,

37

the phytoplankton biomass is spatially distributed according to the direction of the ocean currents, while the regions with the red circles demonstrate no special structure associated with the currents. For the image on the left, the sea surface temperature has a distribution coincident with ocean currents, such as in the locations of the green circles, and not in the regions represented with the red circles.

In the field of horizontal divergence, we can see that the highest velocities are found near the coastal strip (40.40°N and 40.11°N) with values of 0.07 s^{-1} and 0.1 s^{-1}. Also, we record high values of horizontal divergence off the coast with values varying with latitudes, with the maximum velocity of 0.1 s^{-1} being reached at 40.50°N and 40.35°N. We can observe that the low concentration of chlorophyll-a coincides with the lowest values in the SST and with the maximum horizontal divergence.
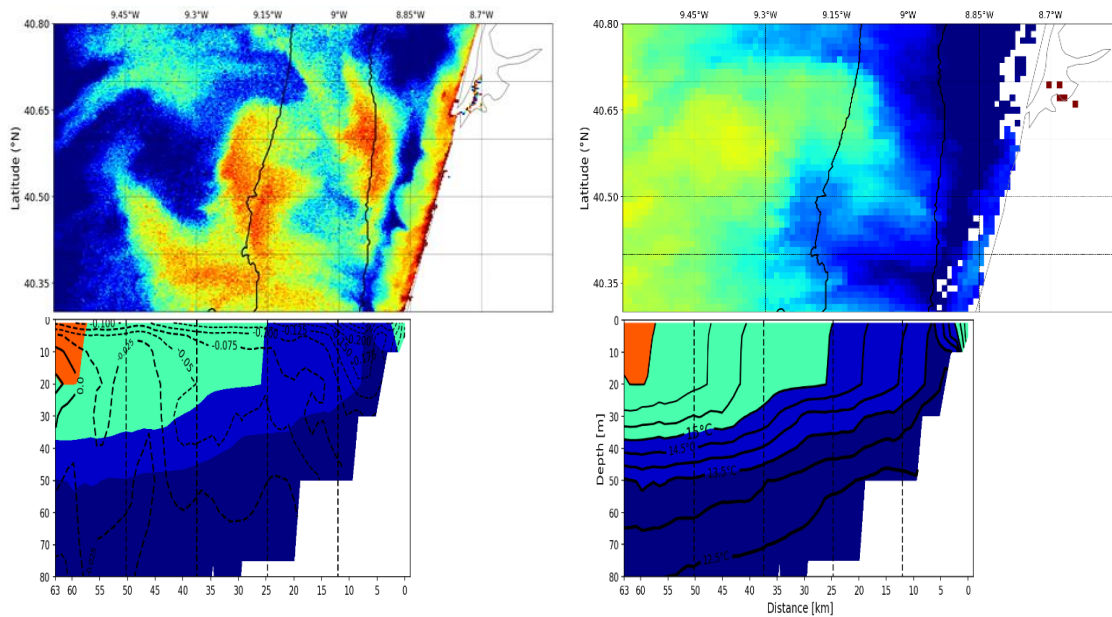
Figure 3.18: The same representation Fig. 3.10, but for the 11th of September.

Ocean currents show variability in intensity, with the highest velocities being close to the coast, with values of -0.250 m/s, and with lower velocities in the open ocean with values of -0.100 m/s. We can see that the currents from 9.60°W and 9.00°W do not present any change in the water column (dashed lines horizontally), however, from 9.00°W to the coast there is a deflection of the ocean currents associated there is the formation of a southward coastal jet. In the case of temperatures at depths, an upwelling of the cooler water layers is observed through the deflection of the temperature lines, with a dimension of 25 km. However, there is a layer of warmer water confined to the coastal region. In the vertical profiles of the currents, we observe a pattern of currents similar to those of September 10th, however the coastal jet moved more offshore. The vertical profile of the temperature has the same structure as on the 10th (same latitude), however, it is greater in extension. It is important to highlight that the area with low concentration of chlorophyll-a coincides with the coastal jet and with the intersection of temperature with the surface.
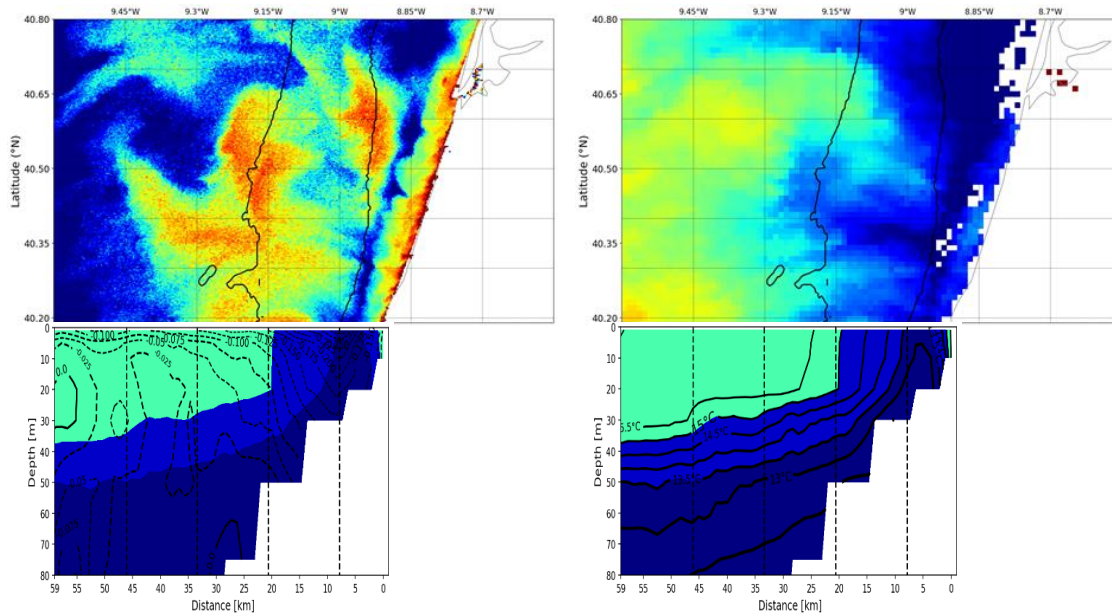
Figure 3.19: The same representation Fig. 3.11, but for the 11th of September.

Ocean currents, at 40.19°N, demonstrate a southern component over the entire depth with a maximum velocity of -0.150 m/s, between 9.15°W and 9.00°W. At these longitudes, we can observe a southward coastal jet fully developed along the coastal region. In the sea temperature image, we observe an extensive body of cold water upwelled with a length of 20 km. It is also verified the existence of the second layer of colder water emerging with a temperature of 13.5°C, at 9.00°W. For the vertical profile of the currents remains similar to those on the 10th, however the coastal jet has lower values on the 11th of September compared to the day before. In the case of temperature, the difference is in the intersection of isotherms (13.5°C) on the surface that does not occur the day before.
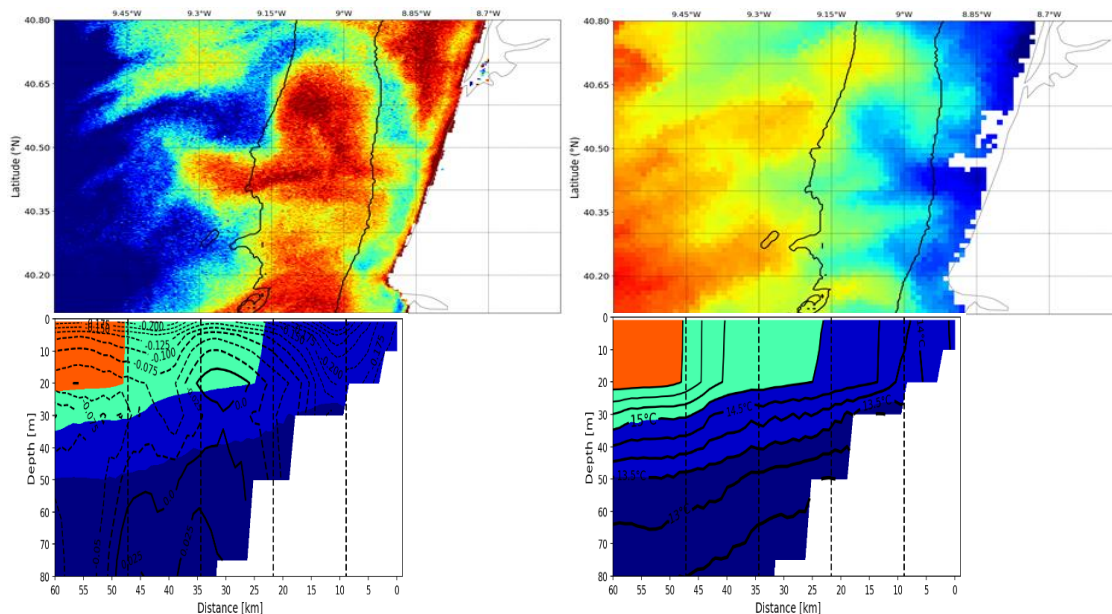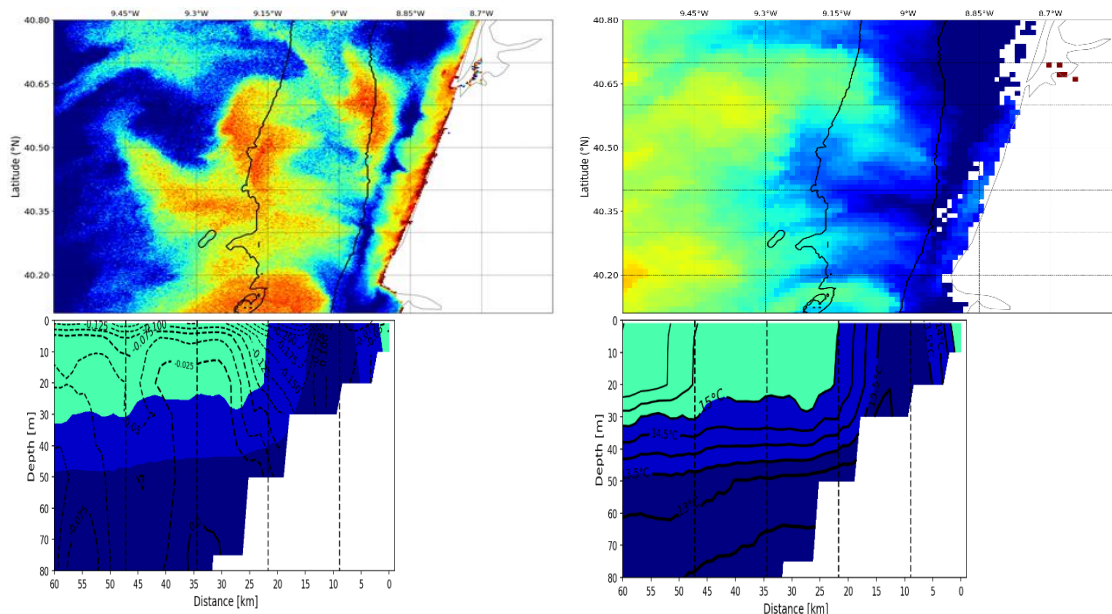

Figure 3.20: The same representation Fig. 3.12, but for the 11th of September.

For the latitude of 40.11°N (South of Cape Mondego), the currents are southward, as the previous latitudes, with maximum speeds of -0.250 m/s being reached between the longitudes of 9.15°W and 9.00°W. The coastal jet observed further north moved to the offshore region and in the coastal region

the ocean currents present lower velocities with values of -0.075 m/s. The sea temperature presents a more intense coastal upwelling compared to previous latitudes. The coldest water mass previously observed for latitude 40.19 exhibits a cross-shore extent, not in agreement with the satellite image. In this case, we were unable to distinguish the coastal jet in the vertical profile from the currents as was possible on September 10th. In vertical profile of the temperature, it has an identical structure for the same latitude as the previous day, but with the presence of a more extensive isotherm (13.5).

4   Discussion

4.1   Processing Levels for Sea Surface Temperature

The L4 satellite data are currently used in oceanography to study oceanic processes because they are complete, both temporally and spatially (Meneghesso et al., 2020). The big difference between these satellite products concerning the others selected (Piscismod Iberia, Chl_NN, Chl_OC4Me, and OC-CCI) is mainly related to the processing level. Since L4 products depend on an interpolation method to fill the missing data due mainly to the cloud cover, they end up temporally, and spatially smoothing the data, i.e., the interpolation performed on L4 products will remove the variability observed in short-scale oceanographic processes (Pereira et al., 2020). Therefore, it would not be possible to observe features like the low chlorophyll-*a* band along the 50 m isobath on September 11, 2019, as it is an oceanographic phenomenon with a small space (5 km), and -time scales (~1-2 days). According to Meneghasso et al., (2020), SST L4 products present an overestimation of the sea surface temperature up to 2°C for regions with intense coastal upwelling, and it is necessary to be careful when interpreting the results obtained. Other studies have shown that L3 products perform better than L4 satellite products. Pereira et al. (2020), observed that L4 satellite products for sea surface temperature in Cape Frio (Southeastern Brazil) had an overestimation of 4°C relative to *in situ* data during a period of coastal upwelling, which could be attributed to the processing performed on the L4 satellite data. Therefore, it was decided not to use satellite data (MUR, and OISST) so as not to introduce errors associated with SST overestimation due the processing level being L4.

4.2   Accuracy in Chl-*a* Retrieval

When performing match-up analyses it is necessary to restrict spatially and temporally, to guarantee a simultaneous comparison between the *in-situ* samples and the satellite pass (Sá, 2013). Normally, the choice of data for *in situ* comparisons must be adapted according to the physical conditions existing in the study sites. However, a very strict selection criterion may reduce the amount of matchups obtained, resulting in a sample with an inadequate statistical result (IOCCG, 2019). Another important aspect focuses on the L2 and L3 data (different processing levels) presenting different matchups and validation results between them. Therefore, L2 data will require higher levels of processing, to attenuate the differences (IOCCG, 2019). One of the processing levels applied to L2 satellite data was the application of different flags to increase data quality (Fig. 2.1). Since there are several factors with the ability to compromise the quality of the match-up (such as the presence of clouds, abnormal atmospheric correction, and pixels without information) (Sá, 2013). One way to reduce errors associated with satellite data is the application of flags (IOCCG, 2019), however, they can reduce the number of possible matchups (Sá, 2013). For the satellite products used, they were not subjected to any additional application of algorithms or an atmospheric correction for data validation.

To understand which would be the best satellite product for the study area, two statistical parameters were applied to assess how the satellite data compared to *in situ* data (Fig. 3.1). The first statistical parameter used was the Room Mean Square, Ψ, allowing the measurement of the data spread. This parameter is often used to quantify data errors or uncertainties (IOCCG, 2007). The second statistical parameter applied was the BIAS, δ, to determine the accuracy of the data, that is, to define the residual offset that remains when positive or negative errors cancel each other out (Sá, 2013). Since Chl-*a* data have a normal distribution when they are log-transformed (Campbell et al., 1995). Then, the same logarithmic transformation was applied to the RMS and BIAS to prevent an incorrect representation of the results (IOCCG, 2007).

The satellite data together with the *in situ* ones showed a reduced number of match-ups due to the application of the flags, being that the maximum reached was for the OLCI (Chl_NN) and Piscismod

41

Iberia with N = 11, followed by the OC-CCI with N = 9 and, finally, the OLCI (Chl_OC4Me) with N = 7. Based on the matchups, chlorophyll-*a* from Piscismod Iberia shows the best performance with a good agreement (r^2 = 0.70), a low dispersion (RMS = 0.27), and an almost non-existent overestimation (BIAS = 0.06). The Chl_NN has a higher agreement than Piscismod Iberia with (r^2 = 0.73), however it exhibits a high dispersion and underestimation of the data (RMS = 0.57, and BIAS = -0.54). The third best performing chlorophyll-*a* product was OC-CCI with a median agreement (r^2 = 0.56), the data show a low dispersion (RMS = 0.32) and an overestimation with the same magnitude as Piscismod Iberia (BIAS = 0.10). The Chl_OC4Me was the product with the worst performance for the study area, presenting a very low agreement (r^2 = 0.37), however the data demonstrate a lower dispersion than Chl_NN (RMS = 0.48), and an overestimation (BIAS = 0.28).

In a study by Delgado et al., (2021), the chlorophyll-*a* neural network product showed good linear regression (r^2 = 0.91) and an underestimation of chlorophyll-*a* concentrations, while the chlorophyll-*a* product OC4Me exhibited a much better linear regression (r^2 = 0.97) and lower errors for the Southwestern Atlantic Ocean. Contrary to the results in the above article, the results presented in this section show the product of Chl_OC4Me with the worst performance in terms of linear regression and higher errors, however the product of Chl_NN is concordant with the results of the article. This performance can be explained by the underestimation of the water-leaving radiance of the OLCI L2 products (Zibordi et al., 2018). In another study carried out by Giannini et al., (2021), for coastal waters in the Northeast Pacific using the 3rd sentinel with the Polymer atmospheric correction algorithm found better performance in the representation of chlorophyll-*a* concentrations compared to the products of satellite-based neural network. Also, note that the Chl_OC4Me product had the worst performance for those coastal waters. The results obtained in the present study are compatible with the results presented by Giannini et al. (2021).

4.3   Evaluation of the ROMS Model

The oceanographic processes observed in Western Iberia due to the influence of coastal upwelling show similar results with other coastal upwelling regions (such as NW Africa) in terms of wind forcing and morphological structures (Fiúza, 1983; Relvas et al., 2007). Fiúza et al., (1982) showed the prevalence of coastal upwelling conditions from July to September, in continental Portugal, due to the intensification of northerly winds during the summer months. In the period studied here (September 2019) (Fig. 3.4) a succession of intensification and relaxation of the along-shore wind component was observed. Figueiras et al., (2002), reiterate how important is the short-time variability existing in the wind field, due to its ability to generate successive episodes of upwelling and downwelling in a period of 15 days.

The satellite-derived SST maps show the presence of subsurface waters confined to the coastal region associated with the first peak of the wind forcing (Fig 3.5a), while for the upwelled waters regress and disappear due to the relaxation of the along-shore wind component (Fig. 3.5b). On the remaining days, there is a regression of the colder waters towards the coastal region due to the relaxation of the wind field. Based on the results, it can be inferred that along-shore winds play an important role in the circulation of the coastal upwelling (Wang et al., 2015) and, depending on, the wind intensity there will be the extent of the upwelled waters (Grifoll et al., 2015). The same behaviour of temperature increase related to wind relaxation and temperature decrease is associated with wind intensification, as stated by Oliveira et al., (2019). According to Lopes et al., (2009, 2014), a difference of 2°C to 3°C can be observed between the cooler waters near the coastal region concerning the warmer waters due to the intensification of the winds from the north, between Figueira da Foz and Porto. The results presented in

Section 3.2.2 show a difference in sea surface temperature between the coastal and oceanic regions, with the same order of magnitude.

During the coastal upwelling, it is observed the existence of several filaments with different dimensions along the study area. According to Haynes et al. (1993), several filaments were formed due to the presence of capes for NW Iberia. However, in a simulation performed by Roed and Shi (1999), the authors observed that the filaments do not depend on shoreline geometry or shelf-slope topography to develop. However, the anchoring of mesoscale structures is associated with irregularities in the shelf-slope topography for the Iberian Peninsula. In another article by Cordeiro el al. (2015), the model suggested that the formed filaments are associated with coastal topography, as observed near Cape Mondego. Therefore, the filaments observed in Fig. 3.5 can be justified by the existence of several mechanisms.

When comparing the satellite data with the model solutions, there is a difference in the representation in the sea surface temperature values, where the model represents the coldest temperature compared to the satellite data. This behaviour can be observed between Figures 3.5 and 3.7, and in the qualitative comparison of the data in which the modelled temperature is represented as lower when compared to the satellite observation. This agrees with what was observed by Kuebel et al., (2006), and Lopes et al., (2009), where the sea surface temperatures represented by the model are usually cooler compared to the *in situ* temperature data. However, the opposite is also true in another model (roms_his_Perc in the Fig. 3.2), where the modelled temperature is substantially higher than the actual temperature represented (satellite data in the Fig. 3.2). The results obtained by the ROMS model present a sea surface temperature comparable to the model in the article by Lopes et al., (2009).

The results demonstrate an evolution of the coastal divergence line to a more offshore region over time, that is, there is a coastal divergence line on the 10th of September, approximately 5 km from the coast. For the 11th of September the coastal divergence moved further offshore (~10 km from the coast). In the model of Austin & Lenz. (2002) it is also observed an evolution of the coastal divergence off the coast, on the East Coast of the United States. The model results initially demonstrate a coastal divergence 10 km from the coast, and, over the remaining days, there is a displacement of the horizontal divergence further out (12 km from the coast). In the end, the final distance represented by the model for the coastal divergence was 20 km from the coast. Based on the results obtained for the displacement of the coastal divergence, they are in agreement with the article by Austin & Lenz. (2002). This observed structure has several impacts on the concentration of Chl-*a* since they serve as a barrier for Ekman transport, that is, it prevents the transport of biological material to the open ocean and vice-versa (Estrade et al., 2008). Thus, it creates an "incubator" for phytoplankton biomass in the coastal region. This will be discussed in more detail in the following sections.

4.4   Distribution of Chl-*a* associated with coastal upwelling

The intensity of the wind field and its temporal variability is an important factor for the formation of phytoplankton biomass in the coastal region (Yokomizo et al., 2010). The results presented here show that the distribution of chlorophyll-*a* concentration typically follow the spatial distribution of sea surface temperature (Fig. 3.5 and Fig. 3.6), i.e., the cooler subsurface waters exhibit the highest concentrations of chlorophyll-*a* (e.g., Moita, 2001).

In September 2019, the highest concentrations of chlorophyll-*a* are present near the coastal region with values of 5 mg/m^3 compared to the oceanic regions with values of less than 1.5 mg/m^3. These results are concordant with Moita, (2001) and Picado, (2016) for chlorophyll-*a* concentrations during the summer. In the first days, there is a higher concentration of chlorophyll-*a* with values above 3 mg/m^3 concerning

the surrounding waters due to nutrients from the River Mondego. It is consistent with the results of Saraiva et al., (2007), where the residence time in the river is of short duration and, therefore, the consumption of nutrients by phytoplankton is carried out in the coastal region.

In Fig. 3.6a) to Fig. 3.7c) different filaments transport the phytoplankton biomass from the coastal region to the oceanic region. Filaments are an important exchange mechanism between coastal and oceanic waters due to their ability to transport biological content (nutrients and Chl-*a*) (Mason et al., 2006). According to Rossi et al., (2013), the filaments are responsible for transporting about 60% of the chlorophyll-*a* in the Iberian upwelling system. In Fig. 3.6d), there is a change in the spatial distribution of chlorophyll-*a* due to the intensification of along-shore winds. For Fig. 3.7e), between Cape Mondego and Ria de Aveiro, it can be seen an initial decrease in chlorophyll-*a* associated with an intensification of the along-shore component. However, the low concentration of chlorophyll-*a* is observed in detail in Fig. 3.6f) related to the highest peak in the wind forcing. In the remaining figures, a uniform distribution of phytoplankton biomass is observed above Cape Mondego due to the relaxation of the upwelling winds, on the other hand, south of Cape Mondego, the low concentration chlorophyll-*a* remains near the coast. This permanence of a strip of very low chlorophyll-*a* may be associated with the presence of Cape Mondego (sudden change in the topography) driving local physical processes. However, Oliveira et al. (2009), reported that the minimum concentrations of chlorophyll-*a* are usually located north of the Capes, which are associated to an increase of both the mixed layer depth and the horizontal velocities.

Using the cross-shore vertical sections of the model, it is possible to evaluate how the spatial distribution of the concentration of chlorophyll-*a* and the temperature of the sea surface is influenced by the intensification/relaxation of the upwelled favourable winds. In the first days, Fig 3.8, there is a gradual decrease in the temperature of the sea surface as it approaches the coastal region and an increase in chlorophyll-*a* associated with upwelled waters. In this case, there is a low-intensity coastal upwelling due to the weak longshore winds. Therefore, the offshore transport of upwelled waters and chlorophyll-*a* is smaller and, thus, confined to the coastal region.

On the 5th and 8th, a more accentuated decrease in temperature towards the coast is observed compared to the previous days. In this case, the concentrations of chlorophyll-a show a gradual increase, however this increase occurs more offshore compared to the 2nd and 4th of September, mainly because the intensification of offshore water transport associated with the increase in wind forcing.

On the 10th and 11th a different behaviour than expected is observed, with a decrease in chlorophyll-*a* in the coastal region that accompanies the decrease in sea surface temperature. This phenomenon happens when the magnitude of the along-shore component of the wind stress is greater than -0.16 N/m^2 creating a spatial asymmetry between the Chl-*a* and the SST. This asymmetry between Chl-*a* and SST was also observed in the paper by Oliveira et al., (2009) during peak wind intensity, but their analysis was focussed on the Chl-*a* patterns around Cape Carvoeiro and Cape Roca. On the remaining days, you can still observe the asymmetry between Chl-*a* and SST on a smaller scale. This decrease, in observed asymmetry, is justified by the decrease in the northerly winds, providing a regression of upwelled waters and a homogenization of the phytoplankton biomass. The difference in chlorophyll-*a* concentrations between the coastal and oceanic regions agrees with the results obtained by Picado (2016).

4.5   Coastal divergence and impacts on phytoplankton biomass

For the 5th, 10th, and 11th of September, it is observed that the spatial distribution of sea surface temperature and chlorophyll-*a* presents a good visual agreement with the ocean currents modelled by ROMS for the coastal regions. However, this visual consistency between modelling and satellite data occurs less frequently in oceanic regions.

In the coastal region, the horizontal divergence can be used to identify the location where the upwelling occurs due to surface divergence in the ocean. It is observed that the maximum coastal divergence is not located in the coastline, but furthermore offshore. Over the days (5, 10, and 11), there is an intensification of the horizontal divergence associated with the wind forcing increase. When comparing the chlorophyll-*a* concentrations with the horizontal divergence, the very low of chlorophyll-*a* concentrations observed between the 9.00°W and 8.90°W matches with the maximum coastal divergence. Despite this, in Fig. 3.9, there is a maximum divergence near Cape Mondego, but we do not find a decrease in chlorophyll-*a* in the same region. Therefore, for a sharp decrease in chlorophyll-*a* to occur, surface divergence velocities must be greater than 0.05 s^{-1}.

In the simulation carried out by Austin & Lentz (2002), it is shown that the cross-shore transport divergence shifts to offshore regions with the evolution of the coastal upwelling. Therefore, the maximum coastal divergence observed offshore agrees with the results of these authors. In the case of day 5, for the vertical representations of sea temperature and velocities with the NS component, there is a tendency for the colder water masses to decrease in-depth due to the along-shore wind that is transporting the masses from cooler waters to the sea. In this case, the currents at depth have a southward component with the highest speeds in the surface associated with the wind.

From day 10 onwards (Fig. 3.14 to Fig. 3.16), it is possible to verify the upwelling of the waters (15.0°C – 13.0°C) with different cross-shore extensions along with the vertical profiles. In this case, from ocean currents there is the formation of a coastal jet with a southward direction related to the upwelled of colder water masses. Similar behaviour is observed for the ocean currents and the temperature at depth for September 11th, but with greater intensity due to the intensification of the wind field. The appearance of the coastal jet for the 10th and 11th of September is related to the intensification of the along-shore winds (Fig. 3.4), as mentioned in the above article. However, the formation of the coastal jet is justified by the maximum coastal divergence in the offshore region, consequently generating intense vertical movements in the water column (Austin & Lentz, 2002) associated with the coastal upwelling. Therefore, this coastal jet is formed in response to the geostrophic balance with the upwelled isopycnals (Huyer, 1983). The coastal jet will act as a barrier preventing the propagation of phytoplankton biomass to the oceanic region (Mason et al., 2006), as shown in Figures 3.13 and 3.17.

5   Conclusion

As this work is based on oceanographic processes with a short time scale (days) it is necessary to select a satellite product with a high spatial resolution and processing level used in the satellite data. A preliminary assessment of the L4 products, which remove short-scale oceanic processes due to spatial and temporal interpolation, showed that there were not appropriate to study of the upwelling episode of NW Portugal in the first half of September 2019. A comparison between *in situ* Chl-*a* observations and various satellites Chl-*a* estimates shown that the best performing satellite product was Piscismod Iberia compared to Chl_NN, Chl_OC4Me, and OC-CCI products. During the study period, an intermittent coastal upwelling associated with intensification and relaxation of the along-shore wind component was observed. The ROMS model was able to realistically represent the sea surface temperature observed by the satellite, albeit with an underestimation of the temperature. The spatial distribution of phytoplankton biomass follows the spatial distribution of sea surface temperature, however, there is an asymmetry between Chl-*a* and SST on 10th and 11th of September. This observed asymmetry is associated with an intensification of the wind forcing in those days. The maximum coastal divergence responsible for the upwelling of subsurface waters occurred in the offshore region and not along the coast. In the cross-shore sections, it was observed that the southward coastal jet is related to the intensification of the along-shore winds and the maximum horizontal divergence is not located at the coastline. On September 5th, this coastal jet was not observed due to weak northerly winds compared to 10th and 11th. The low chlorophyll-a concentration signal is related to the maximum coastal divergence and the southward coastal jet during September 10 and 11, 2019.

References

A, E. S., EUMETSAT, & Management, E. M. (2019). *Sentinel-3 Product Notice – OLCI Level-2 Ocean Colour*. *1*, 10.

Antoine, D., & Morel, A. (1999). A multiple scattering algorithm for atmospheric correction of remotely sensed ocean colour (MERIS instrument): Principle and implementation for atmospheres carrying various aerosols including absorbing ones. *In International Journal of Remote Sensing* (Vol. 20, Issue 9). https://doi.org/10.1080/014311699212533

Antoine. (2010). *Sentinel-3 optical products and algorithm definition. OLCI Level 2 Algorithm Theoretical Basis Document: Ocean Color Products in case 1 water*. 1–31. https://sentinel.esa.int/web/sentinel/user-guides/document-library/-/asset_publisher/xlslt4309D5h/content/sentinel-3-olci-transparency-products-atbd;jsessionid=4CEBDA7C1BADD8A425FA66C259CBE658.jvm1?redirect=https%253A%252F%252Fsentinel.esa.int%252Fweb%252

Arístegui, J., Barton, E. D., Álvarez-Salgado, X. A., Santos, A. M. P., Figueiras, F. G., Kifani, S., Hernández-León, S., Mason, E., Machú, E., & Demarcq, H. (2009). Sub-regional ecosystem variability in the Canary Current upwelling. *Progress in Oceanography*, *83*(1–4), 33–48. https://doi.org/10.1016/j.pocean.2009.07.03

Austin, J. A., & Lentz, S. J. (2002). The Inner Shelf Response to Wind-Driven Upwelling and Downwelling*. *Journal of Physical Oceanography*, 32(7), 2171–2193. https://doi.org/10.1175/1520-0485(2002)032<2171:TISRTW>2.0.CO;2

Bakun, A. (1975). Daily and Weekly Upwelling Indices, West Coast of North America, 1967-1973. *NOAA Technical Reports*, *August*, 124.

Blondeau-Patissier, D., Gower, J. F. R., Dekker, A. G., Phinn, S. R., & Brando, V. E. (2014). A review of ocean color remote sensing methods and statistical techniques for the detection, mapping and analysis of phytoplankton blooms in coastal and open oceans. *In Progress in Oceanography*. https://doi.org/10.1016/j.pocean.2013.12.008

Campbell, J. W. (1995). The lognormal distribution as a model for bio-optical variability in the sea. *Journal of Geophysical Research*, *100*(C7), 13237. https://doi.org/10.1029/95JC00458

Cordeiro, N. G. F., Nolasco, R., Cordeiro-Pires, A., Barton, E. D., & Dubert, J. (2015). Journal of Geophysical Research : Oceans Filaments on the Western Iberian Margin : A modeling study. *J. Geophys. Res. Oceans*, 120, 5400–5416. https://doi.org/10.1002/2014JC010688

Chen, J., Zhang, M., Cui, T., & Wen, Z. (2013). A Review of Some Important Technical Problems in Respect of Satellite Remote Sensing of Chlorophyll-a Concentration in Coastal Waters. IEEE *Journal of Selected Topics in Applied Earth Observations and Remote Sensing*, 6(5), 2275–2289. https://doi.org/10.1109/JSTARS.2013.2242845

Cracknell, A. P. (2018). The development of remote sensing in the last 40 years. *International Journal of Remote Sensing*, 39(23), 8387–8427. https://doi.org/10.1080/01431161.2018.1550919

Cravo, A., Relvas, P., Cardeira, S., Rita, F., Madureira, M., & Sánchez, R. (2010). An upwelling filament off southwest Iberia: Effect on the chlorophyll a and nutrient export. *Continental Shelf Research*, 30(15), 1601–1613.https://doi.org/10.1016/j.csr.2010.06.007

Cunha, Emilia. (2002). Physical control of biological processes in a coastal upwelling system: comparison of the effects of coastal topography, river run-off and physical oceanography in the northern and southern parts of Portuguese coastal waters.

De Boyer Montégut, C. (2004). Mixed layer depth over the global ocean: An examination of profile data and a profile-based climatology. *Journal of Geophysical Research*, *109*(C12), C12003. https://doi.org/10.1029/2004JC002378

Delgado, A. L., Pratolongo, P. D., Dogliotti, A. I., Arena, M., Celleri, C., Cardona, J. E. G., & Martinez, A. (2021). Evaluation of MODIS-Aqua and OLCI Chlorophyll-a products in contrasting waters of the Southwestern Atlantic Ocean. Ocean and Coastal Research, 69, 1–6. https://doi.org/10.1590/2675-2824069.20-003ald

Doerffer. (2010). Sentinel-3 L2 products and algorithm definition OLCI L2 ATBD Ocean Colour Turbid Water. OLCI Level 2 Algorithm Theoretical Basis Document: Ocean Colour Turbid Water. 1-50. https://sentinel.esa.int/web/sentinel/user-guides/sentinel-3-olci/document-library/-/asset_publisher/hkf7sg9Ny1d5/content/sentinel-3-olci-ocean-colour-turbid-water-atbd

Ekman, V. W. On the influence of the earth´s rotation on ocean currents. *Ark. Mat. Astron. Fys.,* 2(11), 1-53, 1905

ESA, & EUMETSAT. (2018). Sentinel-3 OLCI Marine User Handbook Doc. No. EUM/OPS-SEN3/MAN/17/907205; https://www.eumetsat.int/website/wcm/idc/idcplg?IdcService=GET_FILE&dDocName=PDF_D MT_907205&RevisionSelectionMethod=LatestReleased&Rendition=Web

Estrade, P., Marchesiello, P., De Verdière, A. C., & Roy, C. (2008). Cross-shelf structure of coastal upwelling: A two — dimensional extension of Ekman's theory and a mechanism for inner shelf upwelling shut down. Journal of Marine Research, 66(5), 589–616. https://doi.org/10.1357/002224008787536790

Fellous, J., Kawamura, H., & Mitnik, L. (2001). A History of Oceanography from Space. January 2006, 1–31.

Figueiras, F. G., Labarta, U., & Fernández Reiriz, M. J. (2002). Coastal upwelling, primary production and mussel growth in the Rías Baixas of Galicia. *Hydrobiologia*, 484, 121–131. https://doi.org/10.1023/A:1021309222459

Fiuza, A. F. de G., Macedo, M. E. De, Guerreiro, M. R. (1982). Climatological space and time variation of the Portuguese coastal upwelling. *Oceanologica Acta*, *5*, 10

Fiúza, A. F. G. (1983). Upwelling Patterns off Portugal. In Coastal Upwelling Its Sediment Record: Vol. 10 A (pp. 85–98). Springer US. https://doi.org/10.1007/978-1-4615-6651-9_5

Frouin, R., Deschamps, P.-Y., Ramon, D., & Steinmetz, F. (2012). Improved ocean-color remote sensing in the Arctic using the POLYMER algorithm. *Remote Sensing of the Marine Environment II*, *8525*, 85250I. https://doi.org/10.1117/12.981224

Giannini, F., Hunt, B. P. V., Jacoby, D., & Costa, M. (2021). Performance of OLCI Sentinel-3A satellite in the Northeast Pacific coastal waters. *Remote Sensing of Environment*, 256(September 2020), 112317. https://doi.org/10.1016/j.rse.2021.112317

Gordon, H. R., & McCluney, W. R. (1975). Estimation of the depth of sunlight penetration in the sea for remote sensing. *Applied Optics*, *14*(2), 413–416. https://doi.org/10.1364/AO.14.000413

Grifoll, M., A. L. Aretxabaleta, and M. Espino (2015), Shelf response to intense offshore wind, J. *Geophys. Res. Oceans*, 120, 6564–6580.https://doi.org/10.1002/2015JC010850.

Haynes, R., Barton, E. D., & Pilling, I. (1993). Development, persistence, and variability of upwelling filaments off the Atlantic coast of the Iberian Peninsula. *Journal of Geophysical Research*, 98(C12), 22681. https://doi.org/10.1029/93JC02016

Hooker, B. (1995). *SeaWiFS Volume 29 , The SeaWiFS Pigment Algorithm CZCS-Type*. 29.

Hooker, S. B., Reilly, J. E. O., Brien, M. C. O., Siegel, D. A., Toole, D., Menzies, D., Smith, R. C., Mueller, J. L., Mitchell, B. G., Kahru, M., Cota, G. F., Carder, K. L., Frank, M., Harding, L., Magnuson, A., Phinney, D., Moore, G. F., & Aiken, J. (2000). SeaWiFS Postlaunch Technical Report Series Volume 11 , SeaWiFS Postlaunch Calibration and Validation Analyses , Part 3. In *Nasa Technical Memorandum* (Vol. 11, Issue January 2000).

Hu, C., Lee, Z., & Franz, B. (2012). Chlorophyll a algorithms for oligotrophic oceans: A novel approach based on three-band reflectance difference. *Journal of Geophysical Research: Oceans*, *117*(1), 1–25. https://doi.org/10.1029/2011JC007395

Hu, C., Feng, L., Lee, Z., Franz, B. A., Bailey, S. W., Werdell, P. J., & Proctor, C. W. (2019). Improving Satellite Global Chlorophyll a Data Products Through Algorithm Refinement and Data Recovery. *Journal of Geophysical Research: Oceans*, *124*(3), 1524–1543. https://doi.org/10.1029/2019JC014941

Huyer, A. (1983), Coastal upwelling in the California Current system, Prog. Oceanogr., 12(3), 259–284, doi:10.1016/0079-6611(83)90010-1.

J.T.O. Kirk Light and photosynthesis in aquatic ecosystems. 2nd edition, xvi, 509p. Cambridge University Press, 1994. Price £50.00. (1994). *Journal of the Marine Biological Association of the United Kingdom*, *74*(4), 987–987. https://doi.org/10.1017/S0025315400090366

Jackson, T., Sathyendranath, S., & Mélin, F. (2017). An improved optical classification scheme for the Ocean Colour Essential Climate Variable and its applications. *Remote Sensing of Environment*. https://doi.org/10.1016/j.rse.2017.03.036

Kuebel Cervantes, B. T., & Allen, J. S. (2006). Numerical model simulations of continental shelf flows off northern California. *Deep-Sea Research Part II: Topical Studies in Oceanography*, *53*(25–26), 2956–2984. https://doi.org/10.1016/j.dsr2.2006.07.004

Kuenzer, C., Ottinger, M., Wegmann, M., Guo, H., Wang, C., Zhang, J., Dech, S., & Wikelski, M. (2014). Earth observation satellite sensors for biodiversity monitoring: potentials and bottlenecks. *International Journal of Remote Sensing*, 35(18), 6599–6647. https://doi.org/10.1080/01431161.2014.964349

Lopes, J. F., Cardoso, A. C., Moita, M. T., Rocha, A. C., & Ferreira, J. A. (2009). Modelling the temperature and the phytoplankton distributions at the Aveiro near coastal zone, Portugal. Ecological Modelling, 220(7), 940–961. https://doi.org/10.1016/j.ecolmodel.2008.11.024

Lopes, J. F., Ferreira, J. A., Cardoso, A. C., & Rocha, A. C. (2014). Variability of temperature and

chlorophyll of the Iberian Peninsula near costal ecosystem during an upwelling event for the present climate and a future climate scenario. *Journal of Marine Systems*, 129, 271–288. https://doi.org/10.1016/j.jmarsys.2013.07.002

McCarthy, M. J., Colna, K. E., El-Mezayen, M. M., Laureano-Rosario, A. E., Méndez-Lázaro, P., Otis, D. B., Toro-Farmer, G., Vega-Rodriguez, M., & Muller-Karger, F. E. (2017). *Satellite Remote Sensing for Coastal Management: A Review of Successful Applications. Environmental Management*, 60(2), 323–339. https://doi.org/10.1007/s00267-017-0880-x

Mason, E., Coombs, S., & Oliveira, P. B. (2006). An overview of the literature concerning the oceanography of the eastern North Atlantic region. Relatórios Científicos e Técnicos IPIMAR, *Série Digital*, 33, 58. http://sabella.mba.ac.uk/1795/

Moita, M. T. (2001). Estrutura , variabilidade e dinâmica do Fitoplâncton na Costa de Portugal Continental. 273.

Mobley, C. D. (1999). Estimation of the remote-sensing reflectance from above-surface measurements. Applied Optics, 38(36), 7442. https://doi.org/10.1364/AO.38.007442

Moore, G. F., Aiken, J., & Lavender, S. J. (1999). The atmospheric correction of water colour and the quantitative retrieval of suspended particulate matter in Case II waters: Application to MERIS. *International Journal of Remote Sensing*, 20(9), 1713–1733. https://doi.org/10.1080/014311699212434

Morel, A, & Antoine, D. (2011). *ATBD 2.9 - Pigment Index Retrieval in Case 1 Waters*.

Morel, André, Huot, Y., Gentili, B., Werdell, P. J., Hooker, S. B., & Franz, B. A. (2007). Examining the consistency of products derived from various ocean color sensors in open ocean (Case 1) waters in the perspective of a multi-sensor approach. *Remote Sensing of Environment*. https://doi.org/10.1016/j.rse.2007.03.012

Meneghesso, C., Seabra, R., Broitman, B. R., Wethey, D. S., Burrows, M. T., Chan, B. K. K., Guy-Haim, T., Ribeiro, P. A., Rilov, G., Santos, A. M., Sousa, L. L., & Lima, F. P. (2020). Remotely-sensed L4 SST underestimates the thermal fingerprint of coastal upwelling. *Remote Sensing of Environment*, *237*(December 2019), 111588. https://doi.org/10.1016/j.rse.2019.111588

Nayak, R. K., Remote, N., Centre, S., Mishra, S. K., Remote, N., Centre, S., Ghetiya, S., Remote, N., Centre, S., & Nagamani, P. V. (2018). Remote Sensing Application in Satellite Oceanography. *The Indian Geographical Journal*, 93(December-2018), 156–165.

Nolasco, R., Pires, A. C., Cordeiro, N., Le Cann, B., & Dubert, J. (2013). A high-resolution modeling study of the Western Iberian Margin mean and seasonal upper ocean circulation. *Ocean Dynamics*, 63(9–10), 1041–1062. https://doi.org/10.1007/s10236-013-0647-8

O'Reilly, J. E., Maritorena, S., Mitchell, B. G., Siegel, D. A., Carder, K. L., Garver, S. A., Kahru, M., & McClain, C. (1998). Ocean color chlorophyll algorithms for SeaWiFS. *Journal of Geophysical Research: Oceans*, *103*(C11), 24937–24953. https://doi.org/10.1029/98JC02160

Oliveira, P. B., Nolasco, R., Dubert, J., Moita, T., & Peliz, Á. (2009). Surface temperature, chlorophyll and advection patterns during a summer upwelling event off central Portugal. *Continental Shelf Research*, *29*(5–6), 759–774. https://doi.org/10.1016/j.csr.2008.08.004

Oliveira, P. B., Amorim, F. N., Dubert, J., Nolasco, R., & Moita, T. (2019). Phytoplankton distribution and physical processes off NW Iberia during two consecutive upwelling seasons. *Continental Shelf Research*, *190*(August 2018), 103987. https://doi.org/10.1016/j.csr.2019.103987

Penven, P., Debreu, L., Marchesiello, P., & McWilliams, J. C. (2006). Evaluation and application of the ROMS 1-way embedding procedure to the central california upwelling system. *Ocean Modelling*, *12*(1–2), 157–187. https://doi.org/10.1016/j.ocemod.2005.05.002

Pereira-Sandoval, M., Ruescas, A., Urrego, P., Ruiz-Verdú, A., Delegido, J., Tenjo, C., Soria-Perpinyà, X., Vicente, E., Soria, J., & Moreno, J. (2019). Evaluation of Atmospheric Correction Algorithms over Spanish Inland Waters for Sentinel-2 Multi Spectral Imagery Data. *Remote Sensing*, *11*(12), 1469. https://doi.org/10.3390/rs11121469

Pereira, F., Bouali, M., Polito, P. S., da Silveira, I. C. A., & Candella, R. N. (2020). Discrepancies between satellite-derived and in situ SST data in the Cape Frio Upwelling System, Southeastern Brazil (23°S). *Remote Sensing Letters*, 11(6), 555-562. https://doi.org/10.1080/2150704X.2020.1742941

Picado, A. T. (2016). Influência dos processos físicos na produção primária ao longo da costa noroeste da Península Ibérica. 191.

Pineau-Guillou, L., Ardhuin, F., Bouin, M. N., Redelsperger, J. L., Chapron, B., Bidlot, J. R., & Quilfen, Y. (2017). Strong winds in a coupled wave–atmosphere model during a North Atlantic storm event: evaluation against observations. *Quarterly Journal of the Royal Meteorological Society*, *144*(711), 317–332. https://doi.org/10.1002/qj.3205

Pinto, L., Mateus, M., & Silva, A. (2016). Modeling the transport pathways of harmful algal blooms in the Iberian coast. Harmful Algae, 53, 8–16. https://doi.org/10.1016/j.hal.2015.12.001

Pitcher, G. C., Figueiras, F. G., Hickey, B. M., & Moita, M. T. (2010). The physical oceanography of upwelling systems and the development of harmful algal blooms. Progress in Oceanography, 85(1-2), 5–32. https://doi.org/10.1016/j.pocean.2010.02.0

Relvas, P., Barton, E. D., Dubert, J., Oliveira, P. B., Peliz, Á., da Silva, J. C. B., & Santos, A. M. P. (2007). Physical oceanography of the western Iberia ecosystem: Latest views and challenges. *Progress in Oceanography*, 74(2–3), 149–173. https://doi.org/10.1016/j.pocean.2007.04.021

Roed, L. P., & Shi, X. B. (1999). A numerical study of the dynamics and energetics of cool filaments, jets, and eddies off the Iberian Peninsula Lars Petter I and Xiao topographic and / or coastline irregularities, transport in the upper ocean, leading to a persistent physical process. *Journal of Geophysical Research*, 104(Figure 1), 817–841.

Rossi, V., Garçon, V., Tassel, J., Romagnan, J. B., Stemmann, L., Jourdin, F., Morin, P., & Morel, Y. (2013). Cross-shelf variability in the Iberian Peninsula Upwelling System: Impact of a mesoscale filament. *Continental Shelf Research*, 59, 97–114. https://doi.org/10.1016/j.csr.2013.04.008

Saraiva, S., Pina, P., Martins, F., Santos, M., Braunschweig, F., & Neves, R. (2007). Modelling the influence of nutrient loads on Portuguese estuaries. *Hydrobiologia*, 587(1), 5–18. https://doi.org/10.1007/s10750-007-0675-9

Santos, A. (2019). Missão HabWave 2019 - Figueira da Foz. Relatório de Progresso e Trabalhos, REL PT GM 06/12, Instituto Hidrográfico.

Schiller, H., & Doerffer, R. (1999). Neural network for emulation of an inverse model operational derivation of Case II water properties from MERIS data. *International Journal of Remote Sensing*. https://doi.org/10.1080/014311699212443

Schwing, F. B., O 'farrell, M., Steger, J. M., & Baltz, K. (1996). *NOAA Technical Memorandum NMFS COASTAL UPWELLING INDICES WEST COAST OF NORTH AMERICA 1946-95*.

Shchepetkin, A. F., & McWilliams, J. C. (2003). A method for computing horizontal pressure-gradient force in an oceanic model with a nonaligned vertical coordinate. *Journal of Geophysical Research: Oceans*, *108*(3). https://doi.org/10.1029/2001jc001047

Shchepetkin, A. F., & McWilliams, J. C. (2005). The regional oceanic modeling system (ROMS): a split-explicit, free-surface, topography-following-coordinate oceanic model. *Ocean Modelling*, *9*(4), 347–404. https://doi.org/10.1016/j.ocemod.2004.08.002

Steinmetz, F., Deschamps, P.-Y., & Ramon, D. (2011). Atmospheric correction in presence of sun glint: application to MERIS. *Optics Express*, *19*(10), 9783. https://doi.org/10.1364/oe.19.009783

Steinmetz, F., & Ramon, D. (2018). Sentinel-2 MSI and Sentinel-3 OLCI consistent ocean colour products using POLYMER. In R. J. Frouin & H. Murakami (Eds.), *Remote Sensing of the Open and Coastal Ocean and Inland Waters* (Issue October, p. 13). SPIE. https://doi.org/10.1117/12.2500232

Strub, P. T., Kosro, P. M., & Huyer, A. (1991). The nature of the cold filaments in the California Current system. *Journal of Geophysical Research*, 96(C8), 14743. https://doi.org/10.1029/91JC010241

Sutcliffe, A., Brito, A. C., Sá, C., Sousa, F., Boutov, D., & Brotas, V. (2016). *Observação da Terra: uso de imagens de temperatura da superfície do mar e cor do oceano para a monitorização de águas costeiras e oceânicas*.

Wang, Y., R. M. Castelao, and Y. Yuan (2015), Seasonal variability of alongshore winds and sea surface temperature fronts in Eastern Boundary Current Systems, *J. Geophys. Res. Oceans*, 120, 2385–2400. https://doi.org/10.1002/2014JC010379.

Wang, J., Lee, Z., Wei, J., & Du, K. (2020). Atmospheric correction in coastal region using same-day observations of different sun-sensor geometries with a revised POLYMER model. *Optics Express*, *28*(18), 26953. https://doi.org/10.1364/OE.393968

Watson, P. A. G., Christensen, H. M., & Palmer, T. N. (2015). Does the ECMWF IFS convection parameterization with stochastic physics correctly reproduce relationships between convection and the large-scale state? *Journal of the Atmospheric Sciences*, *72*(1), 236–242. https://doi.org/10.1175/JAS-D-14-0252.1

Werdell, P. J., McKinna, L. I. W., Boss, E., Ackleson, S. G., Craig, S. E., Gregg, W. W., Lee, Z., Maritorena, S., Roesler, C. S., Rousseaux, C. S., Stramski, D., Sullivan, J. M., Twardowski, M. S., Tzortziou, M., & Zhang, X. (2018). An overview of approaches and challenges for retrieving marine inherent optical properties from ocean color remote sensing. Progress in Oceanography, 160(November 2017), 186–212. https://doi.org/10.1016/j.pocean.2018.01.001

Wooster, W., Bakun, A. & McLain, D. (1976). The seasonal upwelling cycle along the eastern boundary of the North Atlantic. *Journal of Marine Research*, 34, 131-141.

Zhang, Y., Godin, M. A., Bellingham, J. G., & Ryan, J. P. (2012). Using an autonomous underwater vehicle to track a coastal upwelling front. *IEEE Journal of Oceanic Engineering*, *37*(3), 338–347. https://doi.org/10.1109/JOE.2012.2197272

Zibordi, G., Melin, F., & Berthon, J.-F. (2018). A Regional Assessment of OLCI Data Products. *IEEE Geoscience and Remote Sensing Letters*, 15(10), 1490–1494. https://doi.org/10.1109/LGRS.2018.2849329

Yokomizo, H., Botsford, L.W., Holland, M.D. et al. Optimal wind patterns for biological production in shelf ecosystems driven by coastal upwelling. *Theor Ecol 3*, 53–63 (2010). https://doi.org/10.1007/s12080-009-0053-5